REPUBLIC OF TURKEY
YILDIZ TECHNICAL UNIVERSITY
GRADUATE SCHOOL OF SCIENCE AND ENGINEERING

EXPERIMENTAL AND NUMERICAL (OPENFOAM) INVESTIGATION OF HYDRODYNAMIC RESPONSE FOR SEMI-SUBMERGED FLOATING PLATFORMS

Umutcan İNAL

MASTER OF SCIENCE THESIS
Department of Civil Engineering
Program of Coastal and Port Engineering

Supervisor
Prof. Dr. Yalçın YÜKSEL

June, 2023

REPUBLIC OF TURKEY
YILDIZ TECHNICAL UNIVERSITY
GRADUATE SCHOOL OF SCIENCE AND ENGINEERING

EXPERIMENTAL AND NUMERICAL (OPENFOAM) INVESTIGATION OF HYDRODYNAMIC RESPONSE FOR SEMI-SUBMERGED FLOATING PLATFORMS

A thesis submitted by Umutcan İNAL in partial fulfillment of the requirements for the degree of **MASTER OF SCIENCE** is approved by the committee on 05.06.2023 in Department of Civil Engineering, Program of Coastal and Port Engineering.

Prof. Dr. Yalçın YÜKSEL
Yildiz Technical University
Supervisor

Approved By the Examining Committee

Prof. Dr. Yalçın YÜKSEL, Supervisor
Yildiz Technical University _____

Assoc. Prof. Ferdi ÇAKICI, Member
Yildiz Technical University _____

Prof. Dr. Veysel Şadan Özgür KIRCA, Member
Istanbul Technical University _____

I hereby declare that I have obtained the required legal permissions during data collection and exploitation procedures, that I have made the in-text citations and cited the references properly, that I haven't falsified and/or fabricated research data and results of the study and that I have abided by the principles of the scientific research and ethics during my Thesis Study under the title of Experimental and Numerical (OPENFOAM) Investigation of Hydrodynamic Response for Semi-Submerged Floating Platforms supervised by my supervisor, Prof. Dr. Yalçın YÜKSEL. In the case of a discovery of false statement, I am to acknowledge any legal consequence.

Umutcan İNAL

Dedicated to my family

ACKNOWLEDGEMENTS

I would like to express my deepest gratitude to all those who have contributed to the completion of this thesis.

First and foremost, I am immensely thankful to my supervisor Prof.Dr. Yalçın YÜKSEL for his invaluable guidance, unwavering support, and expertise throughout the entire research process. His insights, constructive feedback, and encouragement have been instrumental in shaping this thesis.

I want to express my sincere gratitude to Assoc. Prof. Ferdi ÇAKICI for his invaluable advice, unwavering patience, and remarkable support throughout this thesis. Their contributions have been crucial to the successful completion of this work, and I am truly grateful for his guidance and mentorship.

I am grateful to Yildiz Technical University for providing the necessary resources and facilities that enabled me to conduct this research effectively. Their contribution has been integral to the successful completion of this thesis.

I would also like to express my sincere appreciation to all the participants who generously contributed their time and expertise to this study.

I would also like to thank Yaren BAHÇE for supporting me in every problem I have had and for always being there for me.

Finally would like to thank my parents, Serpil İNAL and Hüseyin İNAL, for being the most incredible parents I could ever ask for. Your love, encouragement, and support have shaped me into the person I am today. I am forever grateful for everything you have done for me.

Umutcan İNAL

TABLE OF CONTENTS

LIST OF SYMBOLS vii

LIST OF ABBREVIATIONS viii

LIST OF FIGURES ix

LIST OF TABLES xii

ABSTRACT xiii

ÖZET xv

1 INTRODUCTION 1

1.1 Literature Review 1

1.2 Objective of the Thesis 14

1.3 Hypothesis 15

2 WIND ENERGY AND FLOATING OFFSHORE WIND TURBINES 16

2.1 Climate Change and Renewable Energy Resources 16

2.2 Wind Energy 19

2.3 Wind Energy Turbines 22

2.4 Floating Offshore Wind Turbines 24

3 NUMERICAL SETUP 30

3.1 OpenFOAM 30

3.2 Governing Equations 31

3.3 Meshing Strategies for Dynamic Fluid-Structure Interaction Simulations 34

4 EXPERIMENTAL SETUP 38

4.1 Wave Basin 38

4.2 Floating Wind Turbine Model 41

4.3 Measurement Systems 44

4.4 Load Case Description 49

5 NUMERICAL MODELLING **57**
5.1 Introduction 57
5.2 3D Floating Cylinder 57
5.3 OC6 Semisubmersible Study 63
5.4 Present Model 72

6 RESULTS AND DISCUSSION **78**
6.1 Further Recommendations 80

REFERENCES **81**

PUBLICATIONS FROM THE THESIS **84**

LIST OF SYMBOLS

dz	Cell size in z direction
ξ	Damping ratio
ρ	Density
μ	Dynamic viscosity
$\mathbf{p}^*$	Excess pressure
g	Gravitational constant
kg	Kilogram
δ	Logarithmic decreement
s	Second
∇	Three-dimesional gradient operator
$\mathbf{u}$	Velocity field
α	Volume fraction
H	Wave height

LIST OF ABBREVIATIONS

CFD	Computational Fluid Dynamics
DNS	Direct Numerical Simulation
DOF	Degree of Freedom
DTU	Technical University of Denmark
FOWT	Floating Offshore Wind Turbine
GW	Gigawatt
FVM	Finite Volume Method
IEA	International Energy Agency
LES	Large Eddy Simulation
MARIN	Maritime Research Institute Netherlands
MW	Megawatt
NREL	National Renewable Energy Laboratory
NWT	Numerical Wave Tank
PISO	The Pressure Implicit with Splitting of Operators
PSD	Power Spectral Density
PV	Photovoltaic
RE	Renewable Energy
RANS	Reynolds Averaged Navier-Stokes
RAO	Response Amplitude Operator
SIMPLE	Semi-Implicit Method for Pressure Linked Equations
TLP	Tension Leg Platform
URANS	Unsteady Reynolds Averaged Navier-Stokes
VOF	Volume of Fluid

LIST OF FIGURES

Figure 1.1 Multi-turbine model tested in the study of Ishihara et al. . . . 2
Figure 1.2 The platform and wind turbine used in the study of Coulling et al. . . . 3
Figure 1.3 The wind turbine models used in testing were a spar-buoy, a TLP, and a semi-submersible, arranged in a clockwise direction starting from the left . . . 4
Figure 1.4 Plan view of the basin and model experiment . . . 5
Figure 1.5 Scaled SPIC design wind turbine . . . 6
Figure 2.1 Examples of the energy flow pathway from its origin to its ultimate use . . . 17
Figure 2.2 Percentage of renewable energy sources in new power capacity additions across regions . . . 18
Figure 2.3 Historic development of total installations (GW) . . . 20
Figure 2.4 Wind Europe's realistic expectations scenario: new and total (cumulative) installations in Europe . . . 21
Figure 2.5 Early designs for horizontal and vertical axis wind turbines . . 22
Figure 2.6 The evolution of the world's largest commercial wind turbines . . . 23
Figure 2.7 An offshore floating wind turbine platform's degrees of freedom . . . 25
Figure 2.8 Floating platform classification . . . 26
Figure 2.9 The Stability Triangle of Floating Platforms: Approaches to Achieving Static Stability . . . 27
Figure 2.10 Design variations of floating wind turbines . . . 28
Figure 3.1 Vertical section of cylinder showing fixed mesh and background mesh . . . 36
Figure 3.2 Horizontal section of the cylinder with showing different cell types . . . 37
Figure 4.1 Plan view of wave basin . . . 38
Figure 4.2 Overview of wave basin . . . 39
Figure 4.3 EtherCad wave probe system . . . 40
Figure 4.4 Wave probe . . . 40

Figure 4.5 Tripod and wave probe 40
Figure 4.6 1/50 Scale model floating wind turbine 41
Figure 4.7 Sketches of model 42
Figure 4.8 Profile dimensions of model floating wind turbine 42
Figure 4.9 Plan dimensions of model floating wind turbine 43
Figure 4.10 IMU and sensors 44
Figure 4.11 Raspberry Pi panel computer 45
Figure 4.12 Wind generation system overview 45
Figure 4.13 Wind generation drone components 46
Figure 4.14 Load cell system 47
Figure 4.15 Load cell calibrations 48
Figure 4.16 Mooring configuration of floating turbine 48
Figure 4.17 Time series of pitch motion 51
Figure 4.18 Comparison of W8R3 and W8R4 response amplitude operator(RAO)s in pitch motion 52
Figure 4.19 Time series of heave motion 53
Figure 4.20 Comparison of W8R3 and W8R4 response amplitude operator(RAO)s in heave motion 53
Figure 4.21 Pitch time series and PSD of W1 load case 55
Figure 4.22 Heave time series and PSD of W1 load case 56
Figure 5.1 Visualization of 3D cylinder case 58
Figure 5.2 Dimensions and overview of the computational domain 59
Figure 5.3 Mesh resolution of computational domain 59
Figure 5.4 Initial displacement of cylinder 61
Figure 5.5 Heave decay time series of the experimental results of the Palm et al. and the computational results of this study 61
Figure 5.6 Initial pitch rotation of cylinder 62
Figure 5.7 Pitch decay time series of the experimental results of the Palm et al. and the computational results of this study 63
Figure 5.8 Experimental setup of the Robertson et al. 63
Figure 5.9 Computational domain of DeepCWind free decay test simulations 64
Figure 5.10 Mesh resolution of DeepCWind free decay test simulations . . 65
Figure 5.11 Initial position of the DeepCWind heave decay test 66
Figure 5.12 Time series of DeepCWind free heave decay test 66
Figure 5.13 Initial rotation of free pitch decay test 67
Figure 5.14 Time series of DeepCWind free pitch decay test 68
Figure 5.15 Computational domain of DeepCWind semisubmersible for regular wave tests 69

Figure 5.16 Mesh regions and refinement of OC6 semisubmersible case . . 70
Figure 5.17 Time series comparison of the heave, pitch, surge motion and tension force 70
Figure 5.18 RAOs of the heave, pitch, surge motions and tension force of mooring line 71
Figure 5.19 Computational domain of new design semisubmersible turbine for Free Decay Tests 73
Figure 5.20 Mesh resolution of computational domain for free decay tests of new design semisubmersible 74
Figure 5.21 Initial displacement of the platform for heave decay test 75
Figure 5.22 Normalized time series comparison of new design platform free heave decay experiment and numerical output 75
Figure 5.23 Normalized time series comparison of new design platform free pitch decay experiment and numerical output 76

LIST OF TABLES

Table 1.1 Experimental studies of FOWT platforms 7
Table 1.2 CFD examples of FOWT platforms 13
Table 4.1 Hydrodynamic properties of system 41
Table 4.2 Mass and inertia properties for draft = 165 mm 43
Table 4.3 Mass and inertia properties for draft = 275 mm 43
Table 4.4 Mass and inertia properties for draft = 435 mm 43
Table 4.5 free decay test parameters 49
Table 4.6 Irregular wave conditions for model and prototype 49
Table 4.7 Regular wave conditions 50
Table 5.1 Boundary conditions of 3D floating cylinder free decay tests case 60
Table 5.2 Inertial properties of the DeepCwind platform 64
Table 5.3 Comparison of damping and natural periods of OC6 semisubmersible study and this study in heave motion 67
Table 5.4 Comparison of damping and natural periods of OC6 semisubmersible study and this study in pitch motion 68
Table 5.5 Mass and inertia properties for draft = 275 mm 73
Table 5.6 Comparison of damping and natural periods of openfoam and experiment in heave motion 76
Table 5.7 Comparison of damping and natural periods of openfoam and experiment in pitch motion 77

ABSTRACT

Experimental and Numerical (OPENFOAM) Investigation of Hydrodynamic Response for Semi-Submerged Floating Platforms

Umutcan İNAL

Department of Civil Engineering
Master of Science Thesis

Supervisor: Prof. Dr. Yalçın YÜKSEL

Wind energy which is one of the renewable energy sources has an increasing importance in recent years, recognized as a significant solution to global challenges such as climate change and energy scarcity. Since offshore areas with abundant wind resources provide ideal locations for turbine installations, the usage and development of renewable energy devices, such as floating offshore wind turbines (FOWTs), are rapidly growing. However, there is a lack of sufficient experimental and prototype data on the characteristics and reliability of FOWTs. This study aims to contribute to addressing this problem by focusing on the experimental and numerical simulation of a newly designed floating wind turbine platform and validating a numerical wave tank using the OpenFOAM CFD software. Additionally, the study aims to utilize experimental results from the literature and the experimental outputs of present study. Experimental phase of the study comprises of the newly designed 1:50-scaled floating platform model's free-decay, regular and irregular wave tests that were conducted at the Wave Basin of Yildiz Technical University's Hydrodynamics Research Laboratory. For CFD simulations, the OpenFOAM software was used, which employs a finite volume approach to discretize the Unsteady Reynolds-Averaged Navier-Stokes (URANS) equations. The overset mesh method was employed to simulate the dynamic movements of the floating bodies. Initially, the three-dimensional cylinder geometry was validated for free heave and pitch decay cases using experimental data. Then, the open-source FOWT DeepCWind design's free decay tests and dynamic response under regular

wave conditions were simulated and the results were compared with experimental and numerical data found in the literature. Finally, the free heave and pitch decay tests of the new design platform were simulated in OpenFOAM and compared with the experimental results.

Keywords: Floating offshore wind turbine, fluid-structure interaction, OpenFOAM, experimental study

ÖZET

Yarı Batık Yüzer Platformların Hidrodinamik Davranışının Deneysel ve Sayısal (OPENFOAM) Araştırılması

Umutcan İNAL

İnşaat Mühendisliği Anabilim Dalı
Yüksek Lisans Tezi

Danışman: Prof. Dr. Yalçın YÜKSEL

Yenilenebilir enerji kaynaklarından biri olan ve son yıllarda önemi giderek artan rüzgar enerjisi, iklim değişikliği ve enerji kıtlığı gibi küresel sorunlara önemli bir çözüm olarak kabul edilmektedir. Zengin rüzgar kaynaklarına sahip açık deniz alanları, türbin kurulumları için ideal yerler sağladığından, yüzer açık deniz rüzgar türbinleri (FOWT'ler) gibi yenilenebilir enerji cihazlarının bu alanlarda kullanımı ve gelişimi hızla artmaktadır, ancak FOWT'lerin özellikleri ve güvenilirliği hakkında yeterli deneysel veriler ve prototip verileri bulunmamaktadır. Bu çalışmada, yeni tasarlanmış bir yüzer rüzgar türbini platformunun deneysel ve sayısal olarak incelenmesine odaklanılarak bu sorunun giderilmesinde katkıda bulunmak amaçlanmıştır. Bununla birlikte, literatürdeki deneysel ve sayısal çıktılar kullanılarak sayısal dalga tankı doğrulanmıştır. Çalışmanın deneysel aşaması, 1:50 ölçekli yüzer platform modelinin Yıldız Teknik Üniversitesi Hidrodinamik Araştırma Laboratuvarı dalga baseninde yapılan serbest düşüş testleri, düzenli ve düzensiz dalga testlerinden oluşmaktadır. CFD simülasyonları için, Kararsız Reynolds Ortalamalı Navier-Stokes (URANS) denklemlerini diskretize etmek için sonlu hacim yaklaşımı kullanılan OpenFOAM yazılımı aracılığıyla yüzen cisimlerin dinamik hareketlerini simüle etmek için overset mesh yöntemi kullanılmıştır. İlk olarak, serbest dalıp çıkma ve baş-kıç vurma durumları için deneysel sonuç verileriyle üç boyutlu silindir geometrisi doğrulanmıştır. Daha sonra açık kaynaklı FOWT DeepCWind tasarımının serbest düşüş ve düzenli dalga testleri simule edilmiştir. Sonuçlar, literatürdeki deneysel ve sayısal verilerle

karşılaştırılmıştır. Son olarak, yeni tasarım platformunun serbest baş-kıç vurma ve dalıp çıkma testleri OpenFOAM'da simüle edilmiş ve deneysel sonuçlarla karşılaştırılmıştır.

Anahtar Kelimeler: Açık deniz yüzer rüzgar türbinleri, akışkan-yapı etkileşimi, OpenFOAM, deneysel çalışma

1
INTRODUCTION

1.1 Literature Review

Since the availability of computer power is continually rising, the development of numerical wave basins employing CFD is increasing. If properly validated, a numerical wave basin designed by using CFD can be used to design offshore structures in place of or in addition to expensive experimental testing programs. Although the usage and development of renewable energy production sources such as floating offshore wind turbines (FOWT) are becoming inevitable, there is still a lack of data on FOWT in experimental and real-life aspects.

In order to overcome this problem, using a well-validated numerical wave basin can be valuable to create stable and effective FOWT designs. The Navier-Stokes equations provide a mathematical framework for describing the behavior of fluids with viscosity. Unlike potential flow models, the Navier-Stokes equations can account for turbulent and rotational effects, but this increased accuracy comes at a higher computational cost.

The purpose of this section is to provide additional insight into experimental studies, as well as the commonly utilized CFD software tools for fluid-structure interaction, wave modeling, and meshing methods for dynamic structures. Additionally, this section briefly examines relevant studies related to these topics.

1.1.1 Fluid-Structure Interaction Experiments

A new multi-turbine design for a semi-submerged floating structure was proposed in the study of Ishihara et al.[1]. The dynamic response of this structure, which consisted of three turbine towers, was investigated. The model used in the experiment is shown in Figure 1.1. Experiments were performed in a water tank using a 1/150 scale model. The system of mooring consisted of lateral, vertical, and longitudinal springs. Initially, the model was subjected to free decay experiments to determine the natural periods and damping coefficients of the floater during surge, pitch, and heave motions. Then, the response of the floater under regular waves with three distinct wave heights and a range of wave periods was investigated. The dynamic response of the floater under operational and survival conditions was also evaluated. The results indicate that the floater responds minimally under operational conditions and is sufficiently stable under survival conditions. It was discovered that the surge response resonates around the surge natural period and decreases as hydrodynamic damping increases.

Figure 1.1 Multi-turbine model tested in the study of Ishihara et al.[1]

An experimental test of the DeepCwind semisubmersible model was carried out to verify the accuracy of the FAST simulation model developed at the National Renewable Energy Laboratory. The semisubmersible platform was moored using three catenary lines.The platform and turbine used in the study of Coulling et al.[2] is displayed in Figure 1.2. The experimental campaign encompassed a range of scenarios, including steady and dynamic wind conditions, free decay tests under steady wind, simulations of regular and irregular waves, as well as combined wind-wave tests. Second order responses were observed from the experimental test for wave-only cases, which could not be effectively provided by the FAST simulations. Despite this disparity, the overall validation study demonstrated satisfactory performance. To further enhance the simulation's accuracy, it was recommended to incorporate second-order wave diffraction and mooring dynamics physics into the FAST simulation [2].

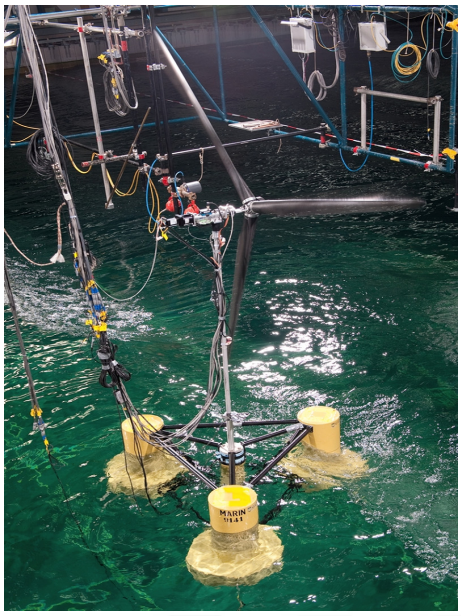

Figure 1.2 The platform and wind turbine used in the study of Coulling et al.[2]

Goupee et al.[3] investigated the behavior of three distinct platform designs for floating wind turbines using scaled model testing in a wave basin at the Maritime Research Institute Netherlands. The experiments were conducted at a 1/50 scale and included the wind turbine along with other components. Figure 1.3 displays images of the various platforms used in the testing process[3].

The experiments simulated the response of a wind turbine that has a 126 m rotor diameter. The wind turbine was connected to three different platforms which are a semisubmersible, a tension leg, and a spar buoy. Free decay tests, irregular wave tests, and dynamic wind tests were conducted. The data obtained from the experimental test were the tension forces of the mooring lines, motions of the platform in 6 degrees of freedom, torque, and displacement of the rotor, and some critical points of the structure. The response of the platforms under three different irregular wave conditions was investigated. Results of irregular wave tests showed that the spar-buoy type of platform had smaller surge displacement, while the TLP platform had smaller pitch rotations. The semisubmersible platform's pitch and surge response in the wave energy frequency range was between the TLP and Spar-buoy platforms, but the semisubmersible platform displayed the largest motion response in the second-order frequencies. Using two distinct dynamic wind cases, the study examined the global wind response of three platform concepts. When there was no wind or when the rotor blades were stopped and feathered in extreme dynamic winds, the response differences between the three systems were essentially identical. This indicated that feathering the rotor blades was an effective strategy for reducing the system's wind load impact. In contrast to the

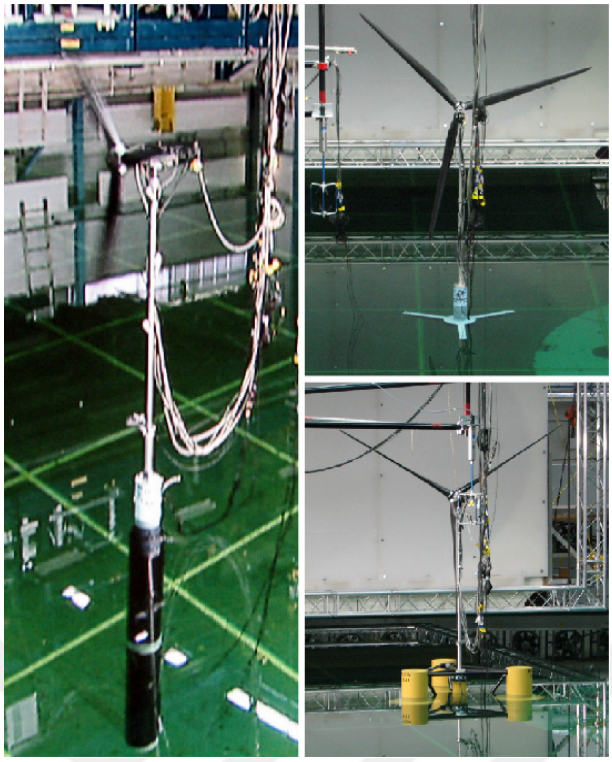

Figure 1.3 The wind turbine models used in testing were a spar-buoy, a TLP, and a semi-submersible, arranged in a clockwise direction starting from the left [3]

feathered scenario, however, the presence of a functioning wind turbine in moderate winds had a considerable impact on the global motion response of the floating wind turbine. Wind loading notably increased the pitch response of the TLP floating wind turbine, but the pitch response energy remained relatively low. The operating wind turbine substantially dampened the response of the structures at the pitch natural frequency, and in the case of the semisubmersible, also at the surge natural frequency. In the frequency domain, the load responses of the TLP (tension-leg platform) mooring system were significantly greater than those of the spar-buoy and semisubmersible designs. Specifically, the TLP mooring load response was found to be about ten times stronger than that of the other designs. Furthermore, although the load responses of the spar-buoy and semisubmersible designs were mostly detected at system surge natural frequencies, the load response of the TLP mooring was substantial at wind energy, wave energy, and associated platform pitch/tower bending natural frequencies[3].

Cao et al.[4] analyzed the dynamic responses of the SPIC floating wind turbine design at a water depth of 60 meters using the basin model testing procedure. The design comprised a DTU 10MW reference wind turbine and a newly developed semi-submersible platform with three slightly slanted side columns. To investigate the operational and short-term radical responses of the design, the researchers

calibrated the wind and wave conditions and identified the model wind turbine system. In order to validate the design and investigate its dynamic responses, a 1:64 Froude scale basin model test was conducted at the Deepwater Offshore Basin of Shanghai Jiao Tong University. Two groups of wave generators were installed adjacent to the basin at a distance of 0.9375 m from the basin's water depth. Figure 1.4 illustrates the plan view of the basin used in the model test[4].

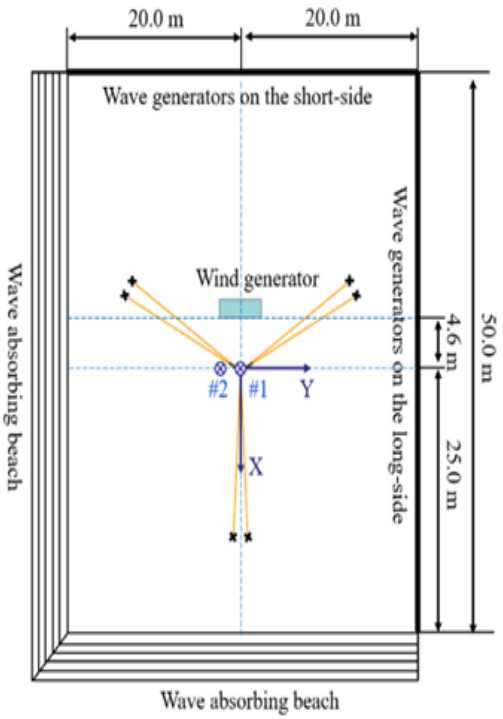

Figure 1.4 Plan view of the basin and model experiment [4]

In order to conduct their study, [4] built a floater model using fiberglass and wood, with a metallic flange made of aluminum alloy connecting it to the sensor at the bottom of the tower. The mass, gravitational center of the structure and inertia components were adjusted by changing the ballast water inside side columns and pontoons below the free surface. Force sensors and accelerometers were used to measure the acting forces and acceleration of the system. In order to measure free surface elevation, wave gauges were used and hot-wired anemometers were used for measuring wind speed. Movements of the system in six degrees of freedom were captured using optical motion capture technology. To keep the platform in place, a mooring system that employs catenary lines were used. Figure 1.5 shows the scaled SPIC design wind turbine used in the study[4].

The natural periods of the six degrees of freedom movements of the SPIC concept wind turbine were determined using free decay experiments. The dynamic behavior of the wind turbine under various operational and extreme conditions, including

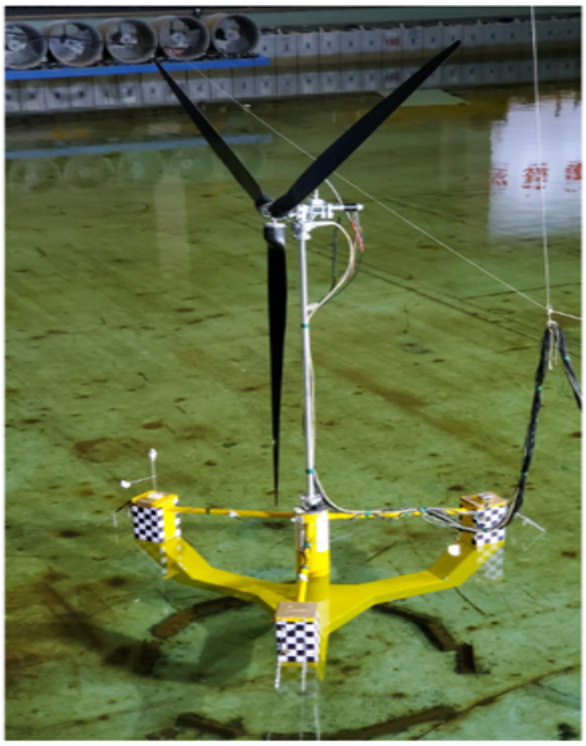

Figure 1.5 Scaled SPIC design wind turbine [4]

wave-only, combined wind-wave, and combined wind-wave-current scenarios, was evaluated using a basin model test. The dynamic behaviors of surge motion, pitch motion, tower-top shear force, tower-base bending moment, nacelle acceleration, and mooring line tension were evaluated and compared under various operating and adverse conditions. Because the natural periods of the six degrees of freedom movements fell outside of the wave period ranges, the SPIC design was able to avoid resonance at wave periods. While the surge resonant response dominated pitch movement, pitch movement was predominantly affected by surge, pitch, and wave-frequency responses. The mean values of the surge and pitch movements were most affected by wind and current stresses. Wind loads were predominantly responsible for the tower-top shear force, the tower-base bending moment, and the nacelle acceleration. Surge motion had an immediate effect on mooring line tension, resulting in the highest mean value under combined wind-wave-current conditions and the highest fluctuation under combination wind-wave conditions. Under combined wind-wave operational conditions, the maximum pitch motion and tower-base bending moment were observed, and the maximum tower-top shear force was not substantially reduced by the presence of current. Extreme values of pitch motion and nacelle acceleration did not exceed the specified limits, indicating that the SPIC concept is suitable for water depths of intermediate depth[4].

The floating test campaign for the OC6 project involved using a simplified model

of the OC5-DeepCwind semisubmersible, which did not have a turbine or rigid tower. The model was fastened to three taut-spring lines and tested for motion decay and wave behavior, including regular and irregular waves. The model's motion amplitudes were monitored during the tests. The experiments were conducted in the Concept Basin of the Maritime Research Institute Netherlands (MARIN). The primary objective of these tests was to provide essential information to project participants to aid them in building and simulating experimental studies. Irregular and regular wave tests and free decay tests in surge, pitch, and heave modes were performed in the study of Robertson et al.[5]. The experimental works given in this section are summarized in Table 1.1.

Table 1.1 Experimental studies of FOWT platforms

Authors	Case	Methodology	Remarks
Isihara et al.[1]	Multi-turbine Semisubmersible, Free decay tests, regular and irregular wave tests, and wind tests	Moored With Springs 6DOF body motions,	Response is minimal under operational stable under survival conditions.
Coulling et al.[2]	DeepCwind Semisubmersible, Free decay tests, regular and irregular wave tests, and steady and dynamic wind , combined wind-wave tests	Catenary Mooring 6DOF body motions,	Conducted in order to validate FAST model.
Goupe et al.[3]	Semisubmersible, a tension leg, and a spar buoy platforms + NREL 5MW Wind Turbine Free decay tests, irregular wave tests, and dynamic wind tests	Mooring line tension force 6DOF body motions, torque, and displacement of the rotor, and some critical points of the structure	Spar-buoy had smaller surge displacement TLP platform had smaller pitch rotations. The semisubmersible platform's pitch and surge response was medium but displayed the largest motion response in the second-order frequencies.
Cao et al.[4]	SPIC floating wind turbine design +DTU 10MW Wind Turbine Wave-only, combined wind-wave, and combined wind-wave-current test were conducted	Force sensors and accelerometers wave gauges hot-wired anemometers Movements of the system in 6DOF were captured using optical motion capture technology. Catenary Mooring	SPIC design's natural period was outside wave period ranges in 6DOF. Turbine's structure's response in the operational and extreme conditions didn't exceed limits.
Robertson et al.[5]	DeepCwind semisubmersible platform only Free decay tests and regular and irregular wave tests	Moored with three springs attached to wires. Mooring tensions and motion of the body in 6DOF are measured.	The aim of this study was to provide data to the participants of OC6 project to give the information needed to simulate and validate numerical models.

1.1.2 CFD Software Tools for Fluid-Structure Interaction

There are various CFD software tools available in the commercial area. The Finite Volume method (FVM) is the most commonly used discretization method used in computational fluid dynamics. Ansys CFD and Star-CCM+ are two of the most common commercial CFD software. This software has been extensively tested and validated in a variety of applications, including multi-phase flows. They're reliable and simple to use, and licenses come with professional support. Both of these software have tools for creating meshing and designing, modules for pre-processing and post-processing. These functionalities allow designers and engineers to create, modify, analyze, and optimize complex designs and simulate their performance under different conditions. The source codes of these tools, on the other hand, are inaccessible, cannot be changed, and are commonly referred to as a "black box." Furthermore, licensing might be costly.

OpenFOAM® is a well-known open-source software used extensively in research circles due to its high level of visibility and easy modifiability. It features a broad selection of integration schemes and solvers, making it suitable for tackling an extensive range of diverse problems.

OpenFOAM is essentially a C++ library that is used to generate executables, sometimes known as applications. There are two types of applications: solvers, which are meant to solve a specific issue in continuum mechanics, and utilities, which are designed to execute data processing tasks. Users with some prior understanding of the underlying approach, physics, and programming techniques involved can design new solvers and tools.[6]

The Interfoam solver is specifically designed to handle multi-phase flows and serves as the basis for several other wave modeling extension solvers.OpenFOAM software and the modified InterFoam solver are used within the scope of this thesis.

1.1.3 Fluid-Structure Interaction Modeling in CFD

Computational fluid dynamics (CFD) is a well-established technique for simulating fluid flow, but using it to model Floating Offshore Wind Turbine (FOWT) platforms is a relatively recent development. Despite its utility, simulating fluid flow around a moving object using CFD remains a challenging and time-intensive task. Since only the fluid domain in CFD meshes, it must be modified as the body moves. This work can be accomplished using a variety of methods.

The morphing or deforming mesh method is the most common and computationally

less costly method. The mesh deforms in response to the transitory motion of a moving body while maintaining the number of mesh cells. As a result, this method is completely conservative. While this method works well for minor body movements, For significant movements, however, the quality of the mesh can decrease dramatically, and the simulation may become unstable and produce divergent results.

In the research of Tran and Kim [7], the overset mesh approach was employed to simulate a free decay test and regular wave tests. The simulation is carried out with the use of the STAR-CCM+ software. The mooring loads were computed using a quasi-static mooring model and a catenary mooring line.CFD simulations were run at full scale. The simulation results were generally consistent with the experimental data. The differences between CFD and the experiment are explained by the fact that the varied Reynolds numbers between the model size and full-scale result in different drag coefficients. The study also showed that performing free decay tests without a turbulence model could yield reliable results. Furthermore, the k-epsilon turbulence model is unsuitable for these simulations because of its major damping.

A benchmark instance of free heave decay of a two-dimensional circular cylinder was designed in the study of Dunbar et al.[8], simulated using the OpenFOAM interDyMFoam solver, and validated by comparing with experimental and theoretical data. Instabilities generated by artificially increased mass, as well as non-physical oscillations in velocity and force. This verified solver was subsequently used to simulate the DeepCwind semisubmersible platform's free heave and pitch decay tests. The simulation results are compared to the NREL FAST/HydroDyn engineering tool. The comparison revealed that at large amplitudes, a significant difference was detected in the heave decay test, which was identified to be associated with viscous effects.

The study of Palm et al.[9] discussed methodology for conducting coupled mooring analysis through the utilization of a two-phase Navier-Stokes (VOF-RANS) model and a high-order finite element model of mooring cables. The technique was developed using OpenFOAM's six-degree-of-freedom motion solver and an in-house mooring code called MooDy. The numerical results were validated by comparing them to experimental data, including decay tests and six cases of regular waves. The surge decay test showed reliable agreement between experimental and numerical results, indicating confidence in the numerical execution of coupling since surge response is entirely determined by the moorings interacting with the body. There was considerable agreement between experimental and computational results, with the coupled numeric model accurately reproducing the wave height

dependency of the response amplitude operators. Overall, the study demonstrates an effective method for coupled mooring analysis that can accurately model the response of a moored, floating vertical cylinder in six degrees of freedom.

Rivera Arreba[10] performed a computational analysis on wave loads acting on floating structures in 2017. The investigation included a cylinder test case and the OC5 project's DeepCWind semi-submersible floating offshore wind platform. OpenFOAM was utilized for the CFD analysis, whereas waves2Foam was used for the wave modeling and mooring model. The numerical wave tank was evaluated to ensure that the generated waves were consistent with theory. The study showed that the motions of the cylinder were correct and that predictions of the motions of the semi-submersible were better than predictions of potential flow. This was true for both nonlinear motions and the ability to capture wave run-up. Rivera-Arreba utilized the interDymFoam and waveDymFoam solvers for fluid-structure interaction and the PIMPLE algorithm for pressure and velocity coupling. A time step with an adjustable value and a maximum value for the Courant number were utilized. A solver that deforms cells but does not permit topological changes in the mesh was used to manage mesh deformation, with a specific region defined for cell movement and deformation. The CFD simulations regarded the flow as laminar and did not account for turbulence.

The study conducted by Bruinsma et al.[11] provides a comprehensive validation of a fully nonlinear numerical wave tank that effectively simulates complex fluid-structure interactions of moored floating bodies. To generate waves within the computational domain, the researchers utilized the interDymFoam solver, which solves the Navier-Stokes equations for dynamic motion in six degrees of freedom, and the waves2Foam toolbox. The simulation was validated using experimental data obtained from the OC5 floating offshore wind turbine and a simple cylinder exposed to waves. The numerical results showed excellent agreement with the experimental data, highlighting the reliability of the simulation and the employed solvers. Additionally, the researchers successfully simulated free decay tests of a two-dimensional horizontal cylinder and the OC5 FOWT platform, achieving a good match with the experimental results. In conclusion, the study demonstrates that the fully nonlinear numerical wave tank can accurately and reliably produce stable numerical solutions for complex fluid-structure interactions [11].

Bruinsma et al.[11] provided a thorough validation of a fully nonlinear numerical wave tank that effectively simulates complex fluid-structure interactions of moored floating bodies. The researchers used the interDymFoam solver, which solves the Navier-Stokes equations for dynamic motion in six degrees of freedom, and

the waves2Foam toolbox to generate waves within the computational domain. Experiment data from the OC5 floating offshore wind turbine and a simple cylinder exposed to waves were used to validate the simulation. The numerical results were in excellent agreement with the experimental data, demonstrating the reliability of the simulation and the solvers used. Furthermore, the researchers successfully simulated free decay tests of a two-dimensional horizontal cylinder and the OC5 FOWT platform, in good agreement with the experimental results. Finally, the study shows that the fully nonlinear numerical wave tank can produce reliable and precise numerical solutions for complex fluid-structure interactions [11].

In the research of Wang et al.[12], the pitch decay motion of the DeepCWind semisubmersible was simulated. The simulation is carried out with the help of the free source CFD application REFRESCO. The 3D linear mooring technique was used, and the results were compared to the experimental data. The deforming mesh discretization method was utilized. The differences in linear damping were moderate, whereas the difference in quadratic damping was significant. The nonlinearity of the mooring line in the experimental setup, which was in catenary form, was connected with this conclusion. It is concluded that the hydrodynamic pressure shifts around the heave plates affect the system's hydrodynamic damping.

In the investigation of Zhou et al.[13] change, the dynamic movement of a semisubmersible platform for varying wave steepnesses was examined. OpenFOAM is used to model the investigation. Five consistently increased wave steepnesses for regular and focused waves were investigated on the floating platform. First, it is determined that focuses waves cause a more violent dynamic response than regular waves. Moreover, it was observed that the nonlinearity of the motion response increased as wave steepness increased.

The study conducted by Chen et al.[14] focused on the development of a numerical wave tank (NWT) that can accurately model wave interactions with complex floating objects undergoing significant motion. The researchers employed the overset mesh technique, which offers several advantages over the moving mesh approach in simulating complex geometries while maintaining a high-quality mesh. The overset mesh approach involves using multiple independent computational meshes that overlap and exchange boundary information during simulation, allowing for the simulation of complex geometries without the need for a single mesh to conform to the geometry's shape. To create the NWT, the researchers integrated the overset mesh method with a wave simulation toolbox in OpenFOAM®, a popular open-source computational fluid dynamics (CFD) software. The numerical wave tank was tested to the test with a variety of

comparison test cases, such as the interaction of 2D regular waves with a floating cylinder and a box-shaped body with superstructures, the entry of a rigid wedge and a section of ship hull into the water, the heave decay of a point absorber wave energy converter, and the motion of a lifeboat in regular waves. Results from the simulations showed that the overset technique is promising for accurately modeling wave interactions with complex floating objects undergoing significant motion. The computed solutions were consistent with experimental data and other reference results in the literature, demonstrating the numerical wave tank's effectiveness in modeling complex geometries in various wave settings. The wedge slamming test case showed that the overset mesh is a feasible and advantageous option for modeling moving bodies with large amplitude movements, which is challenging for the dynamic mesh technique. The researchers found that when a similar mesh resolution is used, the results obtained could be equivalent for both overset mesh and dynamic mesh discretization. However, the overset approach is currently less efficient than the dynamic mesh method due to the additional computational cost of exchanging information between the overlapping meshes. The researchers examined the solver's parallel efficiency and the influence of the overlapping area on solution accuracy and compared their results with dynamic mesh outcomes. While overset mesh may require more computational resources than dynamic mesh, it still provides value for certain fluid-structure interactions despite its inefficiencies.

Wang et al.[15] conducted a verification and validation study to assess the accuracy of computational fluid dynamics (CFD) models for predicting the free-decay motion of the DeepCwind semisubmersible. Multiple institutions provided simulation results to be validated against the experimental data gathered in the OC6 campaign. The objective was to determine if the CFD models accurately estimated the damping coefficients. The study focused on the surge, heave, and pitch-free decay load cases of the floating platform. The damping coefficients and periods of motion were estimated for both CFD simulations and experimental data. The study found that wave radiation had a negligible effect on overall motion damping due to low natural frequencies. The results of the CFD simulations and experiments were in good agreement.Examples of the CFD works given in this section are summarized in Table 1.2.

Table 1.2 CFD examples of FOWT platforms

Authors	Case	Methodology	Remarks
Tran and Kim[7]	DeepCwind semi-submersible with Catenary Mooring Free Decay Regular Waves	STAR-CCM+ Overset Mesh	Free decay simualtions can be conducted without turbulence models. Validated against experiment
Dunbar et al.[8]	2D Circular Cylinder DeepCwind semi-submersible Free Heave Decay	OpenFoam CFD used. InterDyMFoam Solver Morphing Mesh	Validated against theoretical and experimental data. At large amplitudes, a significant difference associated with viscous effects.
Palm et al.[9]	Floating Cylinder with Catenary Mooring Free Decay Regular Waves	OpenFoam CFD used. MooDy code utilized for mooring. Morphing Mesh	The model effectively represents the wave height and dependance of RAO.
Rivera Arreba[10]	DeepCwind semi-submersible 3D Cylinder	OpenFoam Waves2Foam for wave and mooring Morphing Mesh Laminar Flow	For detailed design a fully nonlinear CFD is necessary.
Bruinsma et al.[11]	Two dimensional horizontal cylinder under free decay tests. Moored Decay and Regular wave tests of OC5 FOWT.	OpenFOAM CFD, Waves2Foam tool WaveDyMFoam solver Morphing Mesh	Good agreement with experimental results.
Wang et al.[12]	DeepCWind semisubmersible Free Pitch Decay	REFRESCO CFD used. 3D linear mooring Morphing Mesh	Validated against experiment. Significant Difference in quadratic damping coefficient because mooring was in catenary form in experiment.
Zhou et al.[13]	DeepCwind semi-submersible with Catenary Mooring Regular Waves Focus Waves	OpenFOAM Waves2Foam	Focused waves has more violent dynamic response. Nonlinearity increases with wave steepness.
Chen et al.[14]	Floating cylinder, box-shaped body , a rigid wedge and a ship hull in 2D waves are simulated.	OpenFOAM CFD Overset mesh	Good agreement with experiments. Oversetmesh is a good alternative for dynamic mesh.
Wang et al.[15]	Free decay test of OC6 DeepCwind semisubmersible platform	STAR-CCM+ , OpenFOAM , ReFRESCO CFD softwares are used. Morphing and Overset	Validated against experimental data.

1.2 Objective of the Thesis

Offshore wind turbines offer a promising solution for harnessing wind energy in coastal areas. However, there is still a lack of comprehensive data regarding the behavior of Floating Offshore Wind Turbines (FOWTs) in both experimental and real-life scenarios. To address this gap, the objective of this thesis is to investigate the hydrodynamic behaviors of floating semi-submersible platforms used for wind turbines through numerical and experimental analyses.

The present study employed OpenFOAM, a software that utilizes a finite volume approach to discretize the Unsteady Reynolds-averaged Navier-Stokes (URANS) equations, for the purpose of conducting computational fluid dynamics (CFD) simulations. The floating platforms were simulated using an overset meshing technique, which generated a fixed mesh that is co-moving with the platform within the three-dimensional simulation domain. The study conducted simulations that encompassed free decay simulations of a basic floating cylinder in addition to free decay and regular wave simulations utilizing the semi-submersible geometry of DeepCWind. The obtained results were then compared with existing experimental and numerical results documented in the literature. Additionally, a set of free decay tests was performed using OpenFOAM for a newly designed platform.

In addition to the numerical analyses, an experimental study was conducted on a reduced-scale model (1:50) of the novel design platform in a wave basin located at the hydrodynamic research laboratory of Yildiz Technical University. The model's damping coefficients and natural periods in three degrees of freedom (3 DoF) were assessed through the implementation of free decay tests. Additionally, an examination was conducted on the platform's response to both regular and irregular waves.

The objective of this study is to augment the comprehension of the hydrodynamic properties of semi-submersible platforms for wind turbines by merging numerical simulations and experimental testing. The results of this study will have a significant impact on the enhancement of FOWTs' efficiency and dependability, ultimately promoting the adoption of sustainable wind energy in offshore areas.

1.3 Hypothesis

Based on the study's objectives, it is hypothesized that a thorough investigation of the hydrodynamic behaviors of floating semi-submersible platforms for wind turbines, using both numerical and experimental analyses, will provide valuable insights into their performance and response characteristics. The use of OpenFOAM for computational fluid dynamics (CFD) simulations, in conjunction with the construction of an overset meshing approach, is predicted to accurately capture the dynamic behavior of floating platforms in a variety of settings. This study is expected to evaluate the numerical model's reliability and provide a deeper knowledge of the platform's hydrodynamic response by comparing simulation results with existing experimental and numerical data. Furthermore, it is stated that the damping coefficients, natural periods, and overall responsiveness of the unique design platform will be examined and associated with numerical predictions by experimental testing on a reduced-scale model. Finally, the findings of this study are likely to help enhance the efficiency, dependability, and overall performance of FOWTs, encouraging the greater deployment of sustainable wind energy in offshore areas.

2
WIND ENERGY AND FLOATING OFFSHORE WIND TURBINES

2.1 Climate Change and Renewable Energy Resources

Climate change is one of the twenty-first century's significant challenges. Its most disastrous implications are still avoidable if present energy arrangements are altered. Renewable energy has a huge potential to reduce emissions from fossil fuel combustion and thus climate change. Renewable energy sources, when properly implemented, can aid in social and economic growth, energy access, a secure and sustainable energy supply, and a reduction in the negative consequences of energy provision on the environment and human health [16].

Energy services are essential in all cultures to provide fundamental human needs (such as illumination, food preparation, space comfort, motion, and conversation) as well as to support manufacturing processes. Services related to energy must be secure and have little environmental impact in order for growth to be sustainable. Long-term social and economic growth needs dependable and inexpensive access to the energy resources required to provide important and sustainable energy services. To be ecologically friendly, energy services must have low environmental repercussions and emit low levels of greenhouse gasses [17].

However, according to the Intergovernmental Panel on Climate Change (IPCC) Fourth Assessment Report (AR4), fossil fuels generated 85% of total primary energy in 2004, the same as in 2008. Furthermore, in 2004, fossil fuel combustion accounted for 56.6 percent of the total emissions of greenhouse gases caused by humans [18].

Renewable energy is defined as any kind of energy produced from solar, geophysical, or biological sources and regenerated by natural processes at a rate equal to or greater than its use rate. RE is obtained from continuous or recurring natural energy flows, such as biomass, solar energy, geothermal heat, hydropower, tide, wave energy, and wind energy. Primary energy is converted into an energy carrier (heat, electricity, or mechanical work) and then transmitted into an energy service in a multi-step process. Renewable energy solutions are adaptable and can suit a variety of energy-related needs. Renewable energy can provide electricity, thermal energy, mechanical energy, and fuels to meet a variety of energy needs as can be seen in Figure 2.1.

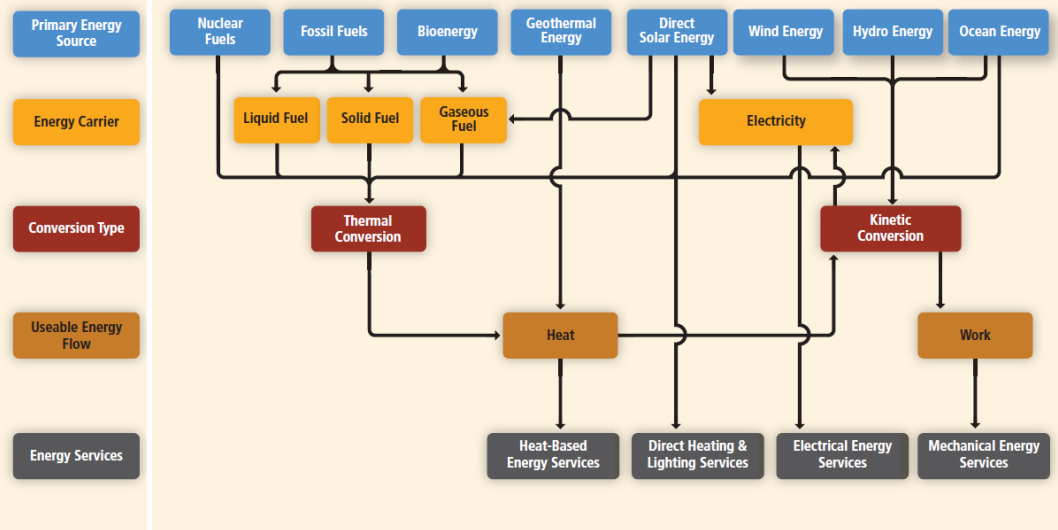

Figure 2.1 Examples of the energy flow pathway from its origin to its ultimate use [18]

According to the International Energy Agency's (IEA) Stated Policies Scenario, the world is predicted to add about 8,500 gigatonnes of additional electricity capacity by 2040. Two-thirds of this additional capacity will come from renewable energy sources, as shown in Figure 2.2 in the aforementioned IEA report [19]. Renewable energy sources account for the bulk of new power capacity additions in most regions, with the European Union and China leading the way, with renewables accounting for approximately 80% of capacity expansions. However, renewable energy accounts for only half of the capacity additions in Southeast Asia and the Middle East. Solar photovoltaic (PV) energy is the leading contributor to new renewable capacity in China and India, followed by wind power, which is the second-largest contributor to renewable energy capacity expansions in many locations. Wind power leads the way in new renewable energy capacity developments in the European Union [19].

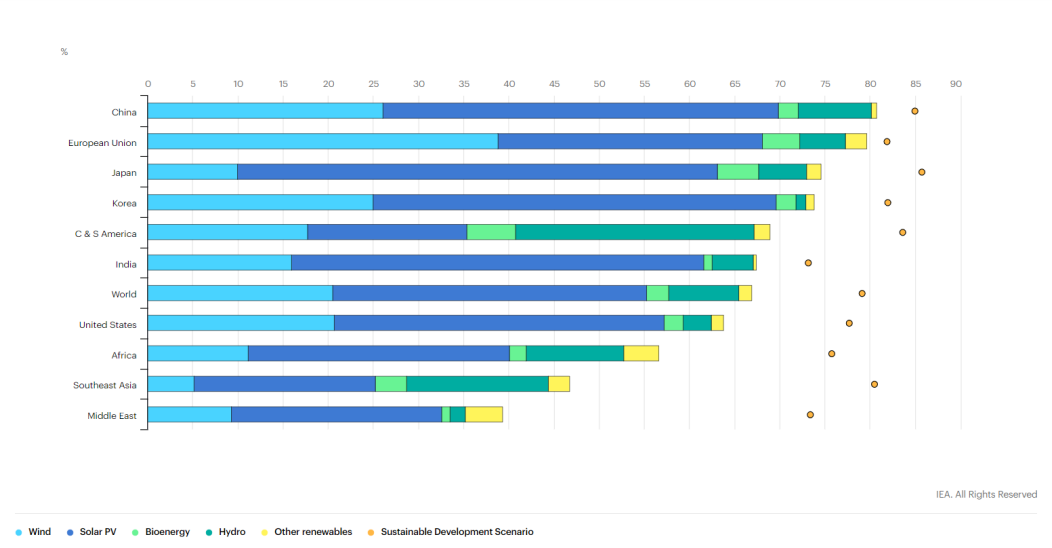

Figure 2.2 Percentage of renewable energy sources in new power capacity additions across regions [19]

2.2 Wind Energy

Wind energy is dependent on the sun's energy in some way. The Earth converts a small portion of the solar radiation it receives into kinetic energy [20]. The fundamental cause of kinetic energy conversion to wind energy is the differential distribution of net incoming and outgoing radiation between high and low latitudes. The location and features of the resulting winds are influenced by a variety of factors, including the Earth's rotation, geography, and temperature changes [21]. To harness wind energy, the kinetic energy of moving air must be converted into usable energy.

Wind energy has been used for thousands of years, with civilizations harnessing its power in various ways. Wind energy has been used for sailing vessels since at least 3,000 BC. Later, wind energy was used for mechanical purposes such as grain grinding, water pumping, and factory machinery, beginning with vertical axis devices and progressing to horizontal axis turbines. Simple windmills were used to pump water in China as early as 200 BC, while vertical-axis windmills were used to grind grain in Persia and the Middle East. Windmills were used in food production in the Middle East by the 11th century, and the idea was carried back to Europe by wandering merchants and crusaders. Beginning in the 1990s, the Dutch and other Europeans modified and adapted the windmill for industrial use, utilizing it to saw wood, produce paper, and drain lakes and marshes [22].

Windmill technology was brought to the New World by settlers in the late 1800s and used to pump water for farms and ranches. Windmills, however, were gradually supplanted and phased out of mechanical use as industrialization and rural electricity took root, first in Europe and later in the United States. Throughout the mid-1900s, wind power was used in rural regions and, in some circumstances, on a greater scale. However, it wasn't until the 1970s that wind power became commercially viable on a broader scale, thanks to technological advances and government support. Denmark was the first to implement small-scale wind power, followed by California in the 1980s, and then Denmark, Germany, and Spain in the 1990s [22].

The worldwide wind sector had its most successful year yet in 2020, with a whopping 53% rise year on year. Despite disruptions in both the global supply chain and project building, the wind energy industry exhibited its resilience by deploying more than 93 GW of wind power. This takes the total global wind power capacity to 743 GW, with 35 GW of the capacity offshore. Figure 2.3, acquired from Global Wind Report [23], also depicts the historical development of total wind power installation between 2001 and 2020.

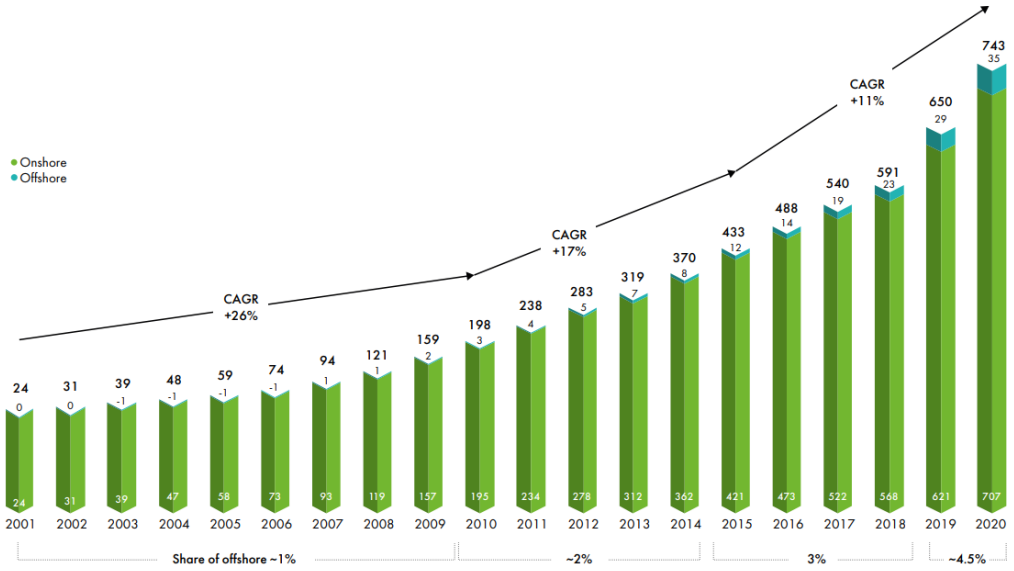

Figure 2.3 Historic development of total installations (GW) [23]

According to GWEC Market Intelligence, approximately 469 GW of new capacity will be installed during the next five years. This equates to a new capacity installation pace of almost 94 GW per year through 2025 [23].

Europe has constructed 220 GW of wind power capacity, with offshore wind accounting for 11% of total capacity. Germany has the most installed capacity in Europe, followed by Spain, the United Kingdom, France, and Italy. Only a few other nations, like Sweden, Turkey, the Netherlands, Poland, Denmark, and Portugal, have more than 5 GW installed. Other countries with more than 3 GW of installed capacity include Belgium, Ireland, Greece, Austria, and Romania [24].

In Wind Europe's Realistic Expectations Scenario, the best estimate of installed capacity in Europe over the next five years is provided. According to this scenario, Europe's total installed capacity will be 341 GW as can be seen in Figure 2.4 [24].

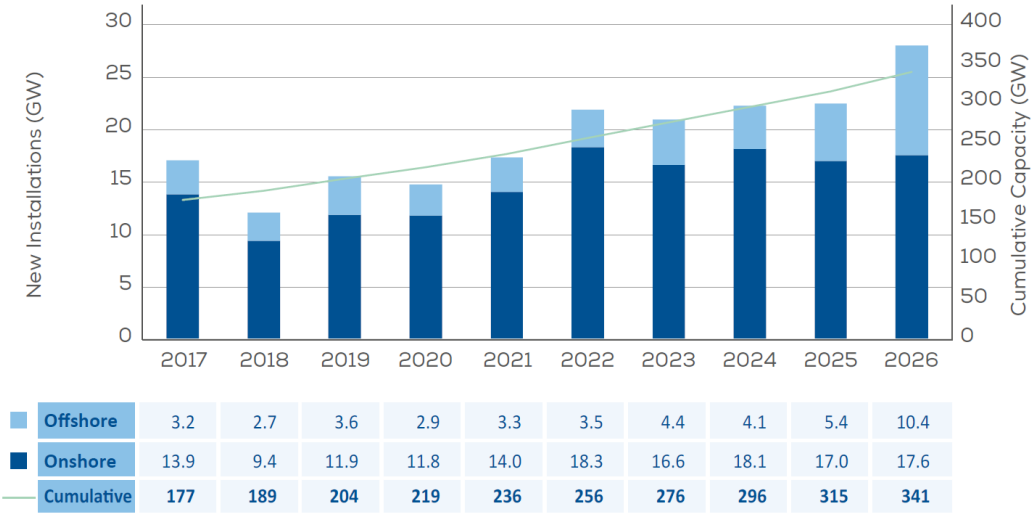

	2017	2018	2019	2020	2021	2022	2023	2024	2025	2026
Offshore	3.2	2.7	3.6	2.9	3.3	3.5	4.4	4.1	5.4	10.4
Onshore	13.9	9.4	11.9	11.8	14.0	18.3	16.6	18.1	17.0	17.6
Cumulative	177	189	204	219	236	256	276	296	315	341

Figure 2.4 Wind Europe's realistic expectations scenario: new and total (cumulative) installations in Europe [24]

2.3 Wind Energy Turbines

Various onshore wind turbine designs with horizontal and vertical axis arrangements were researched in the 1970s and 1980s. Figure 2.5, retrieved from Solar Energy Research Institute [25], depicts several of these designs as sketches.

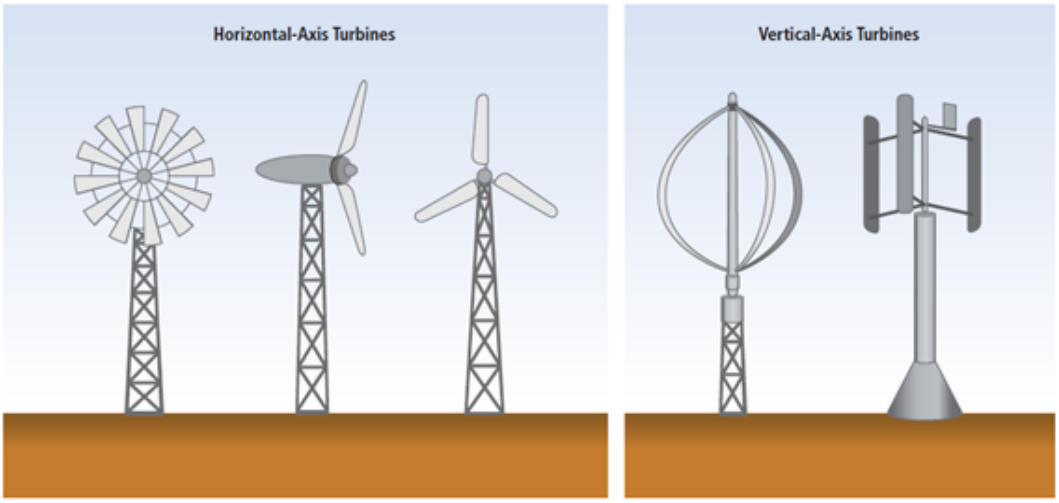

Figure 2.5 Early designs for horizontal and vertical axis wind turbines [25]

Although the horizontal axis design became more prevalent over time, there were still variances in its designs, particularly in the number and direction of blades relative to the tower [26].

Following a period of consolidation, wind turbine designs mostly centered on the three-blade arrangement, with the turbine blades positioned upwind of the tower to avoid the tower blocking wind flow onto the blades [26].

Technology advancements have resulted in a rise in turbine size in terms of tip height and swept area, which has increased their maximum output. Commercially available turbines' tip height climbed from slightly over 100 meters (m) in 2010 (3 MW turbine) to more than 200 meters (m) in 2016 (8 MW turbine), while their swept area expanded by 230 percent. More wind can be caught per turbine thanks to the wider swept area. A 12 MW turbine now in construction is planned to reach 260 meters, approximately 80% of the height of the Eiffel Tower. For 2030, the industry is aiming for even bigger 15-20 MW turbines. The evolution of the world's largest commercial wind turbines and further expectations of this evolution is demonstrated in Figure 2.6 [19].

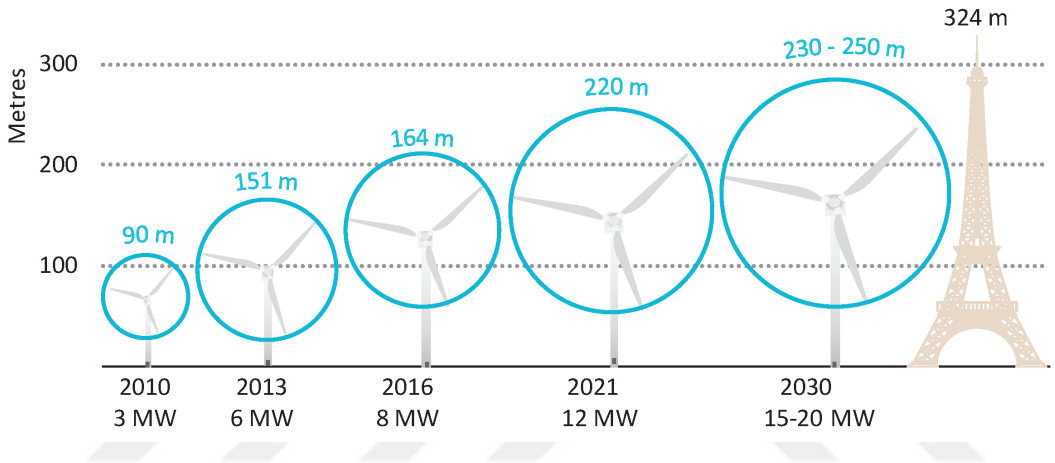

Figure 2.6 The evolution of the world's largest commercial wind turbines [19]

The necessity to minimize the levelized cost of wind energy production by increasing power output has mostly driven the constant rise in turbine size. Taller towers enable access to higher-quality wind resources, and larger rotors allow for more efficient utilization of lower-quality wind resources by increasing the size of the rotors and towers [26].

The potential for further growth in the size of onshore turbines may be limited by a variety of factors, including engineering limitations, material usage constraints, and logistical challenges such as the cost of transporting large components by road and obtaining and using large cranes for installation. Offshore wind turbine design, on the other hand, maybe less constrained by these variables, and hence offshore turbine design considerations are projected to be more relevant in driving the scaling of turbines to bigger sizes in the future[27].

2.4 Floating Offshore Wind Turbines

Wind turbine placement on land is limited by the possibility for noise pollution and aesthetic effect, making it difficult to find acceptable locations. One answer to these problems is to place wind turbines offshore, where the distance from the shore will greatly reduce this issues [28].

Furthermore, offshore wind turbine installation has important advantages such as larger and continuous regions for major projects, higher wind speeds, and less turbulence, resulting in more efficient utilization of the energy resource and reduced fatigue loads on the turbine [29].

As it's mentioned before the wind resource potential of the offshore areas is more abundant at long distances from shore where the water depth is larger than 20 m. Since it's not technically and economically feasible to use bottom-fixed offshore wind turbines at that depths, floating foundations are an attractive concept of solution to install wind turbines at those depths [30].

Over the last two decades, the size of offshore wind turbines has increased significantly. The nominal capacity of each turbine at Vindeby, the world's first offshore wind farm, was only 450kW. However, the global average offshore wind turbine size has climbed to 1.5 MW in 2000, 2.5 MW in 2005, and 6.0 MW by 2020. Offshore wind turbine rotor diameter has also increased substantially in the last 20 years, compared to the first offshore wind turbine, Bonus B35/450kW, installed in 1991. An offshore variant with a rotor diameter of 220 meters built in Rotterdam set the world record for rotor diameter in 2019. Nonetheless, the search for larger turbines continues, with new concepts with a capacity of 15 MW and a rotor diameter of 222 meters expected to become commercially available in 2024 [23].

2.4.1 Degrees of Freedom of FOWT

The interaction of wind and ocean wave conditions makes the stability of floating offshore wind turbines (FOWT) difficult. Due to dynamic excitation, the combination of wind and wave dynamics can generate excessive motion in all six degrees of freedom (6-DOF). These linear and rotational modes of motion are visualized in Figure 2.7[31].

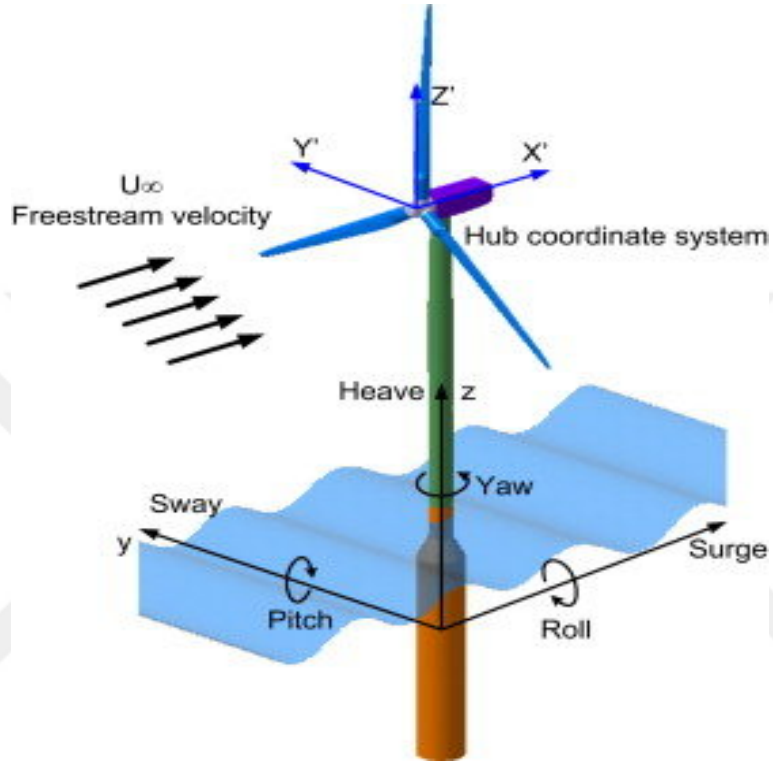

Figure 2.7 An offshore floating wind turbine platform's degrees of freedom [31]

The impact of each move along each of the six degrees of freedom (6-DOF) on the performance of a floating offshore wind turbine (FOWT) must be analyzed and understood. This type of analysis helps in the optimization of FOWT's overall system architecture. Excessive motions in each of the six degrees of freedom (6-DOF) are caused by the dynamic coupling of wind-ocean wave conditions. As a result, it is vital to characterize the impacts of each motion on the overall performance of the system.

2.4.2 FOWT Classification

Based on the physical mechanism employed to establish static stability, FOWT platforms are broadly classified into three types: ballast, mooring line, and buoyancy stabilized platforms [30].

The illustration of floating platform classification along with the semi-submersible design can be seen in Figure 2.8 [32].

To ensure stability, ballast-stabilized platforms use heavy weights suspended from a central buoyancy tank. This weight provides considerable inertial resistance to pitch and roll motions, as well as enough draft to compensate for heave motion [30].

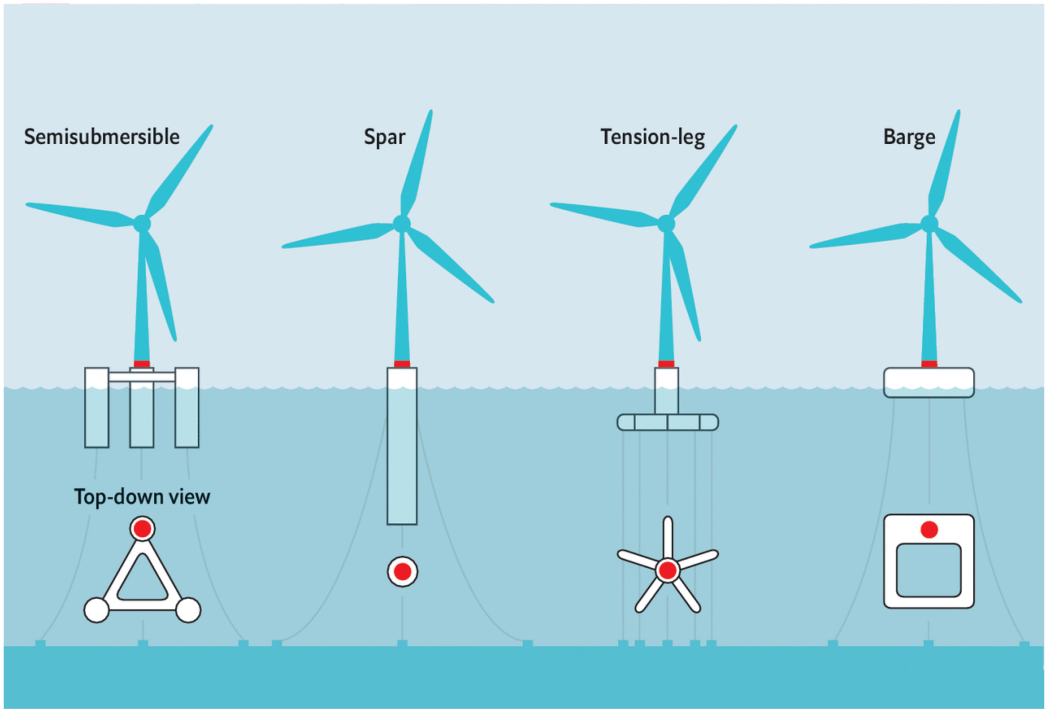

Figure 2.8 Floating platform classification [32]

Platforms with mooring lines achieve stability by the tension of their mooring lines. The Tension Leg Platform (TLP), seen in Figure 2.8, is supported by the tension in its mooring lines. Buoyancy stabilized platforms, on the other hand, use dispersed buoyancy, as seen in Figure 2.8, where the barge uses its waterplane area to regulate the moment [30].

The Floating Platform Stability Triangle which can be seen in Figure 2.9.The stability triangle retriever from the study of Butterfield et al. [30] is a construct that illustrates the relationship between each of the idealized floating platform ideas.

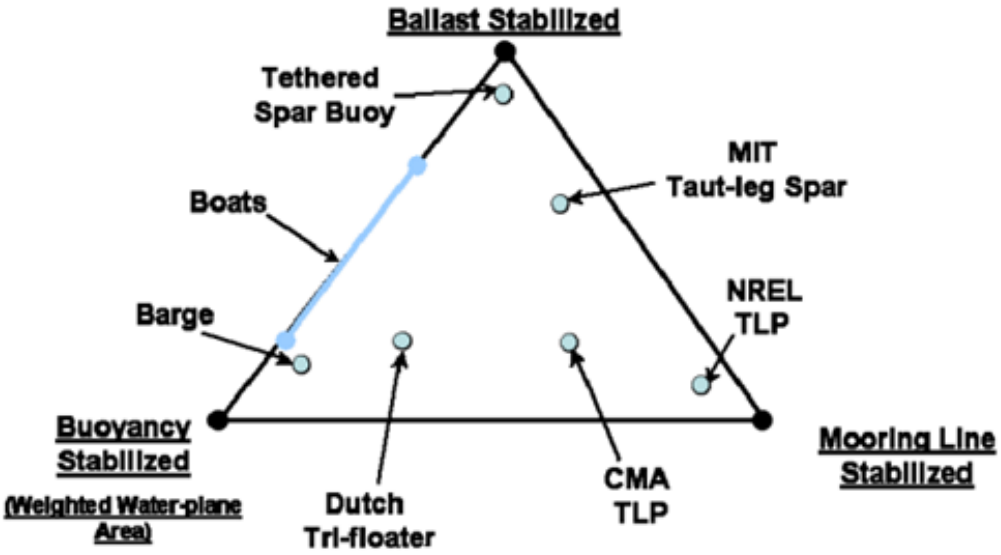

Figure 2.9 The Stability Triangle of Floating Platforms: Approaches to Achieving Static Stability [30]

A buoyancy system is required for all platform types. Because of its basic design, a barge is expected to have the lowest cost per unit of displacement due to well-established production procedures. However, because the barge is mostly supported by a water plane area, it will most likely be a large structure. The spar-buoy is likely to be a simple rolled steel construction, but the extra weight of the ballast necessitates greater displacement, resulting in a high total material cost for the system. The TLP tank is expected to have the smallest displacement needs and the lowest cost, but the tank construction must be more sophisticated to handle the mooring line loads.

The cost of mooring lines is heavily influenced by the depth of the water. Catenary mooring lines connected to drag-embedded anchors are likely to be seen on a barge or a spar buoy. Long lengths are required to avoid vertical loading on the anchors in such a system, which drives the cost of the lines and chain. Because TLPs stretch vertically, their lines will be short, but they must carry a significantly heavier weight to maintain consistent tension between the anchors and the buoyancy tank.

In actuality, all floating designs are essentially hybrid designs that achieve static stability through a combination of all three ways but rely on one major source for stability. Physical hybrid floating platform designs will almost primarily be found between the major points of the triangle. Designers will look for the "ideal" platform

based on a unique mix of stability options that provides the best functionality at the lowest cost [30].

The tri-floater and the semi-submersible are two other support systems widely discussed for floating supports for offshore wind turbines, each using one or more of the three principles illustrated. A tri-floater is a structure made up of columns connected by truss or pipe beams. With a small waterplane field, this provides the benefit of a large second moment of inertia. Semi-submersible platforms have been widely embraced in the oil and gas industry, and as a result, there is a wealth of data on its complex behavior at sea [33].

The semi-submersible is a free-surface stabilized structure with a shallow draft. In comparison to the spar style structure, the semi-submersible's waterplane area leads to better stability efficiency in pitch and roll motions [34].

Robertson [35] conducted an extensive dynamic-response analysis of six alternative offshore floating wind turbine ideas. The same 5-megawatt turbine was used in all six models, but the platforms were diverse, including a barge, a semisubmersible, two tension-leg platforms, and a spar buoy at varying depths. These platform modifications are depicted in Figure 2.10.

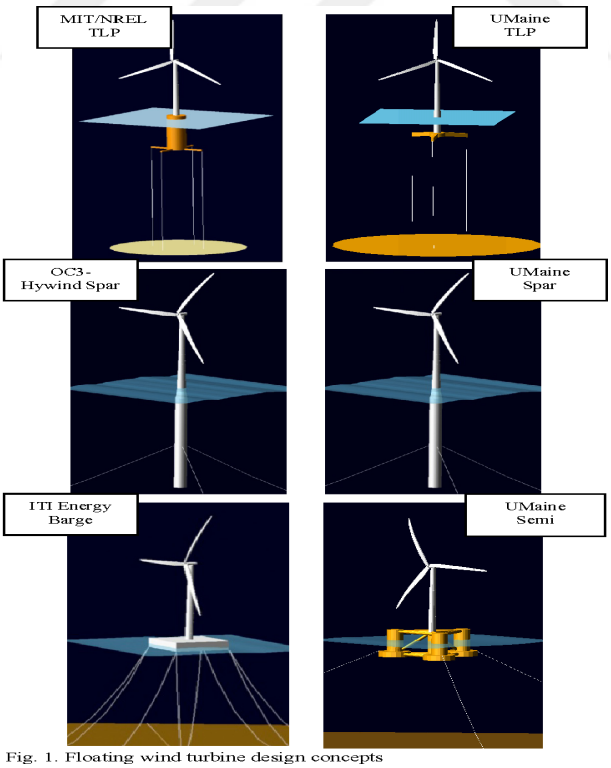

Figure 2.10 Design variations of floating wind turbines [35]

Several floating platforms, including two TLP systems (MIT/NREL TLP and UMaine TLP), an OC3-Hywind spar buoy at different depths (320 m and 200 m), a

UMaine semi-submersible, and an ITI Energy barge, were analyzed by Robertson [35]. All of these platforms were designed expressly for carrying the 5-MW system's rotor, nacelle, and tower.

To summarize, all floating wind turbines put a greater load on turbine components than land-based counterparts, necessitating improvements to assure their safety and durability. Among the six designs studied, the ITI Energy barge exhibited the highest platform motion-induced ultimate and fatigue loads. Despite having distinct structures, the two TLP systems showed identical responses, demonstrating that the strategy to stabilizing the floating system had a greater impact on its dynamics than design details. Despite having lower loads in the tower, the TLP systems demonstrated no significant variations in ultimate and fatigue loads as compared to the spar and semi-submersible systems. Finally, simulating the OC3-Hywind system at a lesser depth had no apparent impact on system dynamics. These findings have significance for floating wind turbine system design and optimization [35].

3
NUMERICAL SETUP

3.1 OpenFOAM

Understanding a floating structure's behavior in a real sea state is just as difficult as determining its efficiency and resistance. Analyzing forces, flow directions, velocities, rotations, and displacements is necessary for the design of modern floating structures. In the past, these analyses were typically conducted in towing tanks, but in recent years, computational fluid dynamics (CFD) methodologies have advanced considerably. These methodologies can now serve as an alternative to or even a replacement for physical experiments, providing cost and efficiency advantages. Several software has been introduced, one of which is open-source: OpenFOAM allows designers to incorporate a modern CFD approach into their design process without making large investments.

Because of its numerous advantages, OpenFOAM has become a popular choice in both academia and industry. One of the benefits of adopting OpenFOAM is that it is open-source software, which allows users to alter the code to match their individual needs. Furthermore, throughout the last decade, OpenFOAM has undergone ongoing development, resulting in the deployment of numerous numerical modules and libraries. These advances have made it simple to create additional libraries and solvers, increasing the popularity of OpenFOAM in both academia and industry. For these reasons, OpenFOAM was chosen for this project.

This section provides an overview of the mathematical models that OpenFOAM uses for FOWT applications. It discusses the fluid flow equations and approaches for capturing free surfaces in two-phase fluid flow.

3.2 Governing Equations

3.2.1 Fundamental Equations of Fluid Dynamics: Navier-Stokes and Continuity Equations

The concepts of mass, momentum, and energy conservation control fluid flows. The concept of incompressible fluids is frequently employed in practical coastal engineering applications. The RANS equations are mathematical expressions that govern fluid flow and link pressure and velocity. They are made up of continuity and mass conservation equations.

$$\nabla \cdot \mathbf{u} = \mathbf{0} \tag{3.1}$$

where **u** is the velocity field in Cartesian coordinates. The Navier-Stokes equations provide a fundamental framework for describing the momentum conservation principle in the context of a Newtonian fluid. This equation is given as:

$$\rho \frac{\partial Du}{\partial Dt} = \frac{\partial \rho \mathbf{u}}{\partial t} + \rho \mathbf{u} \cdot \mathbf{u} = -\mathbf{p}^* - \mathbf{g}\chi\rho + \rho\mu^{\mathbf{2}}\mathbf{u} \tag{3.2}$$

where $\nabla = (\partial_x, \partial_y, \partial_z)$ is the three-dimensional gradient operator, **u** is the velocity field in Cartesian coordinates,**g** is the gravitational constant, and p^* equals $p + \rho g z$ represents the excess pressure. The viscosity μ and the local density ρ are determined in terms of the water and air volume fractions which are defined as α (subscripts a and w), and are formulated as:

$$\rho = \alpha\rho_w + \rho_a\,(1 - \alpha) \tag{3.3}$$

$$\mu = \alpha\mu_w + \mu_a\,(1 - \alpha) \tag{3.4}$$

3.2.2 Finite Volume Method and OpenFOAM

To discretize fluid mechanics equations on a mesh of control volumes, OpenFOAM employs the co-located finite volume approach. Unknown quantities, such as pressure, velocity, or phase fraction, are kept at the center of each cell in this method. This allows the governing equations for each cell to be solved while taking into account boundary conditions and source terms. The numerical scheme used to discretize each term of the governing equations has a substantial impact on the simulation's accuracy, stability, and processing efficiency. As a result, it is critical to select a suitable numerical scheme for each term based on the problem characteristics and computational resources available.

OpenFOAM's interFoam solver is intended to simulate two-phase incompressible flow. This method employs a hybrid of two numerical algorithms, MULES and PIMPLE. The MULES algorithm is used to solve the advection equation determining the phase fraction field at each time step. A multidimensional universal limiter with an explicit solver is used to solve this equation. The MULES algorithm is effective for dealing with complex geometry and fast flows. The momentum and continuity equations are solved using the PIMPLE loop once the phase fraction field is known. The Pressure Implicit with Splitting of Operators (PISO) and Semi-Implicit Method for Pressure Linked Equations (SIMPLE) techniques is combined in the PIMPLE algorithm. This method is very beneficial for dealing with high-pressure gradients and other linearizations that occur in two-phase flow simulations. The PIMPLE algorithm calculates the velocity-pressure coupling. This is accomplished by solving the momentum equation and pressure correction equation iteratively until a solution that meets a defined convergence condition is discovered. A looping parameter that imposes the maximum error on the pressure, velocity, and phase fraction fields governs this iterative operation. To assure numerical stability in simulations, OpenFOAM allows users to specify a fixed time step or a maximum Courant number. The Courant number is a parameter without dimensions that characterizes the stability of a numerical method for solving partial differential equations. It is defined as the velocity multiplied by the ratio of the time step to the characteristic length scale of the problem. To avoid numerical instability, the maximum Courant number is the upper limit that should not be exceeded.

3.2.3 Turbulence Models in CFD

3.2.3.1 Direct Numerical Simulation (DNS)

Direct Numerical Simulation (DNS) is a computational fluid dynamics technique that solves the Navier-Stokes equations numerically, resolving all relevant scales of

motion from the largest to the smallest, which is defined as the Kolmogorov length scale. The Kolmogorov length scale can be obtained when the Reynolds number (Re) is equal to 1. However, due to the absence of any simplifying assumptions, DNS is computationally expensive, with its processing cost increasing with the cube of the Reynolds number. As a result, DNS is generally impractical for simulating engineering flows using current technology.

3.2.3.2 Large Eddy Simulation (LES)

Large Eddy Simulation (LES) is a computational fluid dynamics technique that is more efficient than DNS. In LES, the most energetic turbulent scales (the inertial range of the energy cascade) are resolved explicitly, while the smaller scales are modeled or filtered. The result is a reduction in computational cost while still providing a good representation of the dominant features of the turbulent flow. Furthermore, except in boundary layers, LES simulations are independent of Reynolds number, making them more versatile than DNS. LES is commonly used in engineering simulations to study complex turbulent flows, such as those found in aircraft engines or combustion chambers. However, the computation cost of LES is still usually prohibitive for ordinary simulations.

3.2.3.3 Reynolds Averaged Navier Stokes (RANS)

The RANS turbulence model is a prevalent methodology in the field of fluid dynamics. It is designed to simulate turbulent fluctuations while exclusively resolving mean flow structures. Furthermore, this approach has the capability to incorporate the impact of gradual and unstable phenomena via the utilization of Unsteady Reynolds-Averaged Navier-Stokes (URANS) method. However, hybrid methodologies, such as zonal coupling and detached eddy simulations, have been developed to integrate RANS and LES (Large Eddy Simulation). Both Reynolds-Averaged Navier-Stokes (RANS) and Large Eddy Simulation (LES) are founded on mathematical frameworks that entail a greater number of unknown variables than equations. The Reynolds stress tensor is utilized in RANS to represent the unknowns that are grouped together. Empirical approximations, known as turbulence models, are necessary to solve the aforementioned equations. The models under consideration incorporate supplementary equations, which may be either algebraic or differential in nature, in order to facilitate the resolution of the system. The Shear Stress Transport (SST) model is frequently utilized in external flows and wind turbine applications. The model in question is a formulation of eddy viscosity that incorporates differential equations governing the transport of turbulent

kinetic energy and specific dissipation rate. The SST model is a hybrid formulation that combines the Wilcox k model, which is known for its efficacy in the vicinity of the wall, with the k model, which is known for its efficacy in regions away from the wall. Whilst LES demands greater computational resources, and higher fidelity tools, the SST model offers a satisfactory balance between computational cost and accuracy.

3.2.4 Volume of Fluid Method for Multiphase Modeling

The VOF methodology is employed by the OpenFOAM® software package for the purpose of solving the aforementioned equations given by Hirt and Nichols[36]. The methodology employed in this study entails the utilization of a scalar function $\alpha \in [0\ .1]$ to discern the fluid phase present in every individual cell. Specifically, a value of 0 denotes the presence of air, while a value of 1 signifies the presence of water. Upon utilizing the modified transport equation introduced by Rusche[37], the scalar function undergoes temporal advancement subsequent to the establishment of velocity.

$$\frac{\partial \alpha}{\partial t} + \nabla \cdot u\alpha + \nabla \cdot u_r \alpha \left(1 - \alpha\right) = 0 \tag{3.5}$$

where u_r denotes an artificial velocity, commonly referred to as compression velocity. The last part in the equation above is a numerical diffusion-counteracting artificial compression term that is only active in the interface zone[37].

MULES (multi-dimensional limiter for explicit solution) is a technique used to enforce the confinement of the phase field in a multi-phase fluid simulation. This limiter guarantees that the value of α is between 0 and 1.

3.3 Meshing Strategies for Dynamic Fluid-Structure Interaction Simulations

Despite the CFD is used widely to simulate fluid flows, performing it for the fluid-structure interaction is still difficult and time-consuming since the structure is moving due to the fluid. In CFD simulations, only the fluid domain is typically meshed. As a result, the mesh must be adapted to capture the motion of any structures present in the simulation. Various techniques are available to achieve this goal.

3.3.1 Morphing Mesh Method

The mesh morphing method is a widely used technique in which the cells of the mesh are deformed to accommodate the movement of a body within the fluid domain. This approach is effective for small-scale body movements. However, when larger movements occur, this method can lead to a substantial deterioration in mesh quality, potentially resulting in divergent calculations.

3.3.2 Remeshing Method

Generating a new mesh at every time step characterizes the remeshing approach. This technique demands a high-performance meshing module that guarantees the quality of the mesh at every time step. On the other hand, for bodies with limited degrees of freedom, the sliding meshing method is more efficient. To employ this method, a mesh zone surrounding the body must be established, and interpolation is carried out at the boundary with the global mesh.

3.3.3 Overset Mesh Method

The overset mesh approach is the last method which is used in this study. Two meshes different meshes are created in this method. In typical practice, the global domain is discretized with a fixed mesh, while a separate body-fixed mesh surrounds the floating body, allowing it to move in conjunction with the body's motion. Interpolation between these two meshes is performed at each time step to create a single solution. One of the key benefits of this approach is that it preserves the quality of the mesh during the simulation and avoids mesh deformations. This method is particularly effective when simulating substantial body displacements.

The OpenFOAM overset framework is a general implementation for using unconnected (also known as Chimera) meshes. Meshes, both static and dynamic, are supported. There are no connections between the meshes (background and overset). The overset method is especially beneficial in circumstances when mesh motion and interactions are significant. It avoids the issues and instability that deforming meshes cause.

A background (fixed) mesh is initially constructed in this manner, as illustrated in the purple Figure 3.1. The body is then surrounded by a separate mesh which is defined as overset mesh. Figure 3.1, the fitted mesh is shown in green. The body-fixed mesh surrounding the floating body must encompass the entire body and can assume any shape, but it cannot undergo deformation. Similarly, the global mesh used to represent the overall domain is also non-deformable. Therefore,

their quality remains constant throughout time. Because it is easier to create, the fitted mesh in this study is always rectangular. In order to maintain high-quality interpolation between the two meshes, it is important to maintain a certain number of cells between the outer boundary of the body-fixed mesh. As seen in Figure 3.1, these two meshes are overlapped on top of each other once they've been constructed.

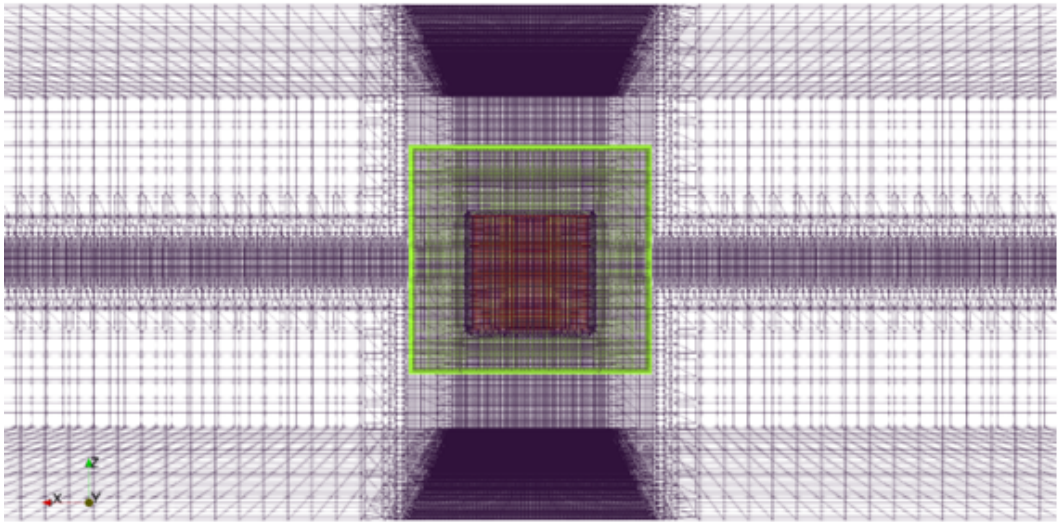

Figure 3.1 Vertical section of cylinder showing fixed mesh and background mesh

The overset method is a numerical approach that entails resolving partial differential equations on both the background mesh and the overset mesh. The computational domain is modified by identifying and removing cells in the background domain that correspond to the interior of the overset domain. These cells are referred to as "holes" and are depicted in Figure 3.2 as red cells. Subsequently, the governing partial differential equations are solved for the extant cells, which are discerned as computed cells (depicted as blue cells in the illustration). The interpolated values for the white cells are derived through the process of interpolation from neighboring elements in the second domain. This involves utilizing background elements for overset elements and vice versa. The utilization of this methodology facilitates the effective emulation of intricate geometries through the partitioning of the domain into smaller, intersecting sub-domains, each possessing its individual mesh.

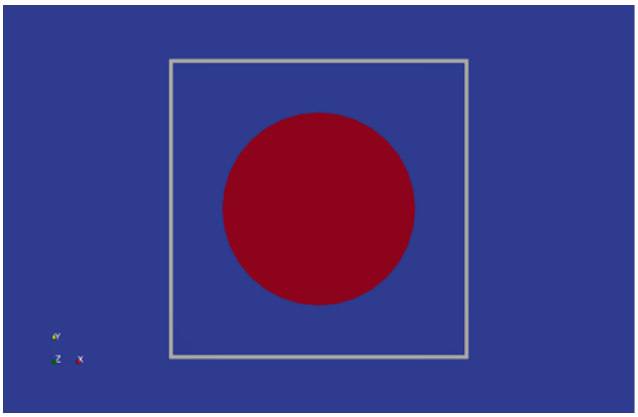

Figure 3.2 Horizontal section of the cylinder with showing different cell types

4
EXPERIMENTAL SETUP

4.1 Wave Basin

The experiments were carried out in the 30.43 m long, 28.85 m wide and 2.20 m deep wave basin (Figure 4.1 and Figure 4.2) in Yıldız Technical University “Hydrodynamics Research Laboratory".

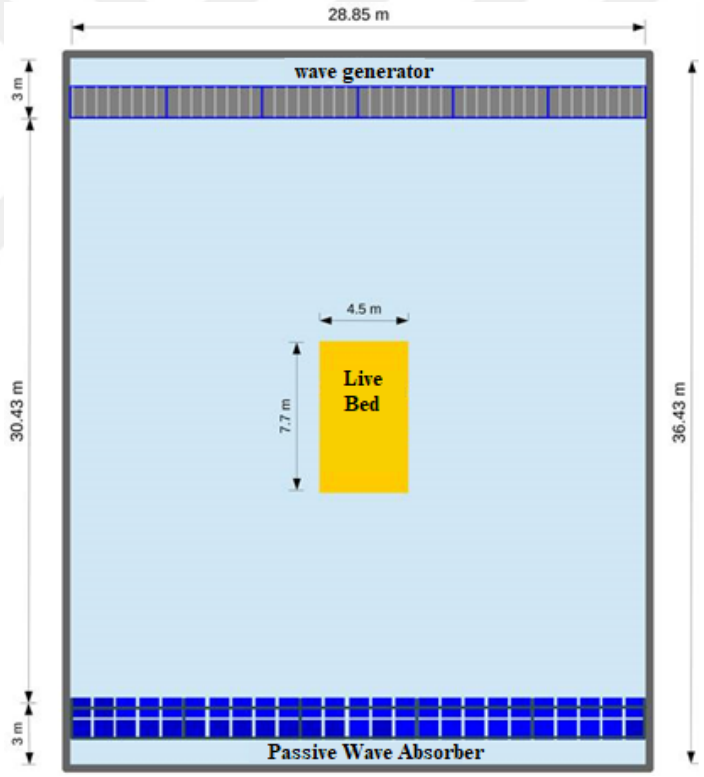

Figure 4.1 Plan view of wave basin

The wave basin is equipped with a 48 pedal piston type wave generator designed by HR Wallingford, which can generate multidirectional waves. The wave generator is capable of producing regular, irregular long and short crest (directional) waves and it has active reflection damping to dampen the reflected wave energy. The total length of the piston type regular/irregular directional wave generator is 28.80 m, and there are 6 modular units, each 4.8 m long. Each wave generator module has 8

pallets, each 60 cm wide (maximum stroke: 3.35 m).

In addition to the active reflection damping function of the wave generator, there is also a passive damper that can be adjusted according to the water depth. The parabolic type passive wave damping system, which can be adjusted according to the depth, is located on the opposite side of the wave generator.

The wave generator is capable of producing JONSWAP, Pierson-Moskowitz, Bretschneider, ITTC, Darbyshire coastal and offshore, Neumann, BTTP, Pink type spectra.

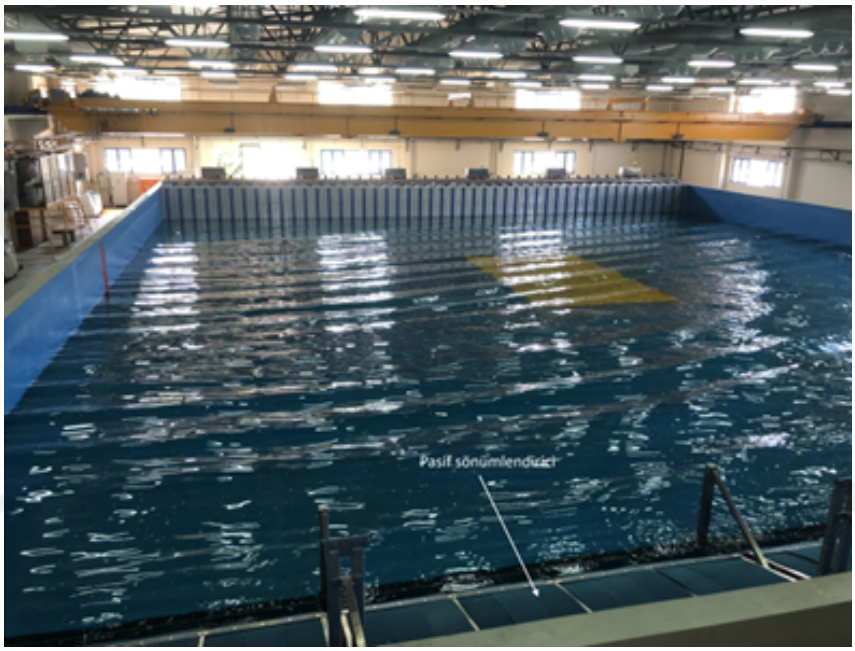

Figure 4.2 Overview of wave basin

EtherCat wave probe system model HR Wallingford AAK2150-RT024-R01-00 was used for wave measurements (Figures 4.3 and 4.4). Four wave probes were placed on the tripod and positioned in the basin (Figure 4.5) also to analyze the reflection due to the floating system. The measured wave was analyzed with the HR DAQ software.

Figure 4.3 EtherCad wave probe system

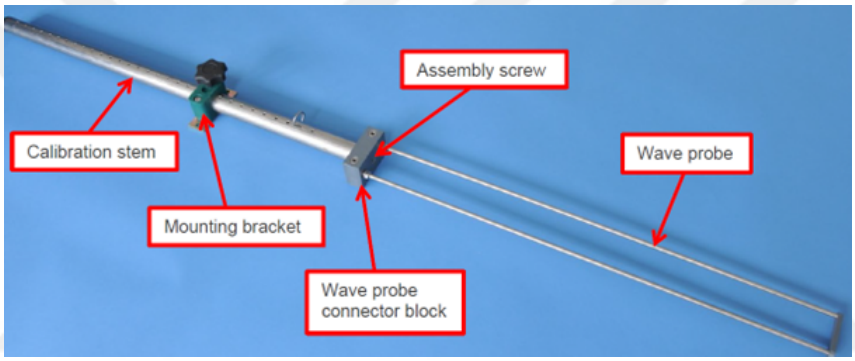

Figure 4.4 Wave probe

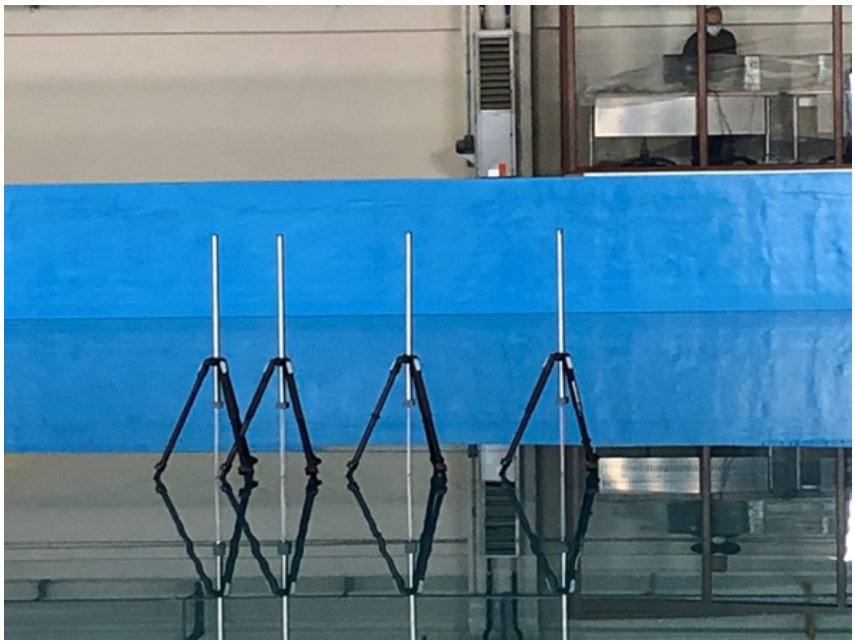

Figure 4.5 Tripod and wave probe

4.2 Floating Wind Turbine Model

The floating wind turbine model seen in Figure 4.6 is semi-submersible and connected to the bottom at three points. The conceptual model scale was chosen as 1/50. Model dimensions are shown in Figures 4.7a,4.7b, 4.8 and 4.9.

The first set of experiments was conducted for three different drafts which are 165 mm, 275 mm, and 435 mm in model scale, 8.25 m, 13.75 m, and 21.75 m in full scale. Mass and Inertia properties of the system for considered drafts are summarized in Table 4.2, Table4.3, and Table 4.4 respectively. Hydrodynamic Properties of the system are given in Table 4.1.

Figure 4.6 1/50 Scale model floating wind turbine

Table 4.1 Hydrodynamic properties of system

Property	Units	Model Scale	Full Scale
Water Depth	m	1	50
Water Density	kg/m^3	1000	1000

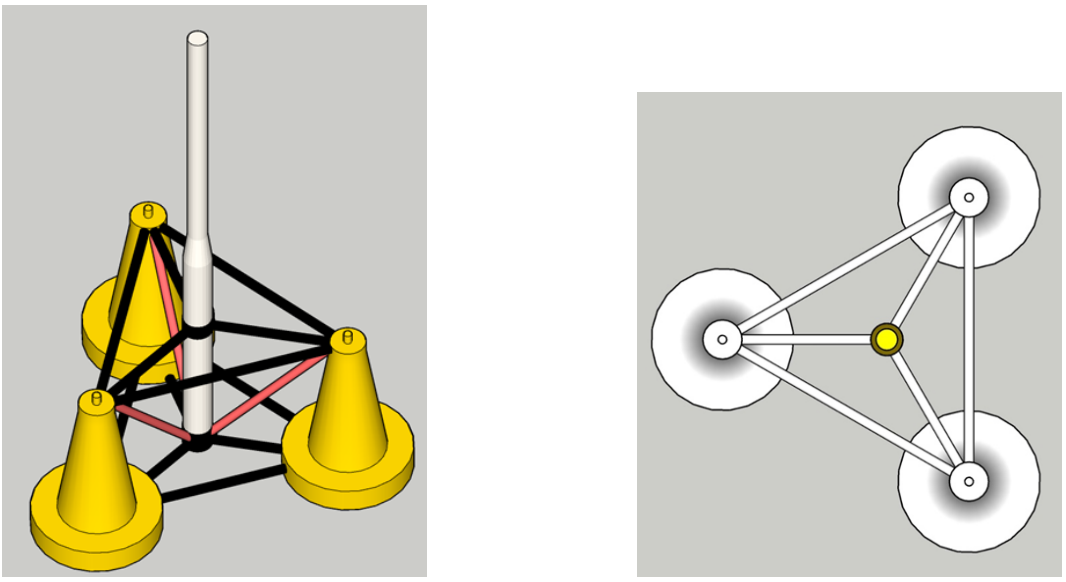

(a) 3D Sketch of Model **(b)** Plan View of Model

Figure 4.7 Sketches of model

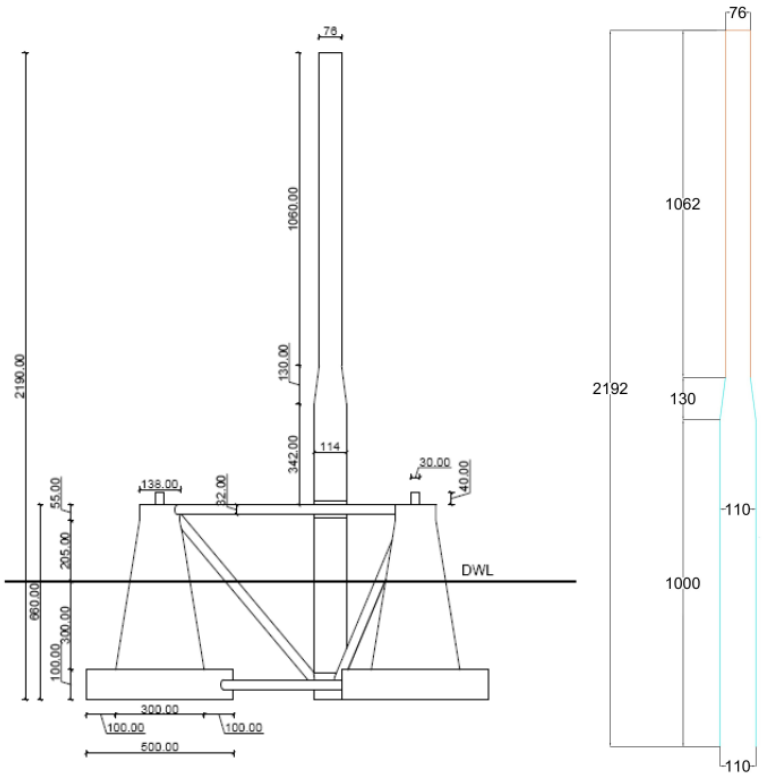

Figure 4.8 Profile dimensions of model floating wind turbine

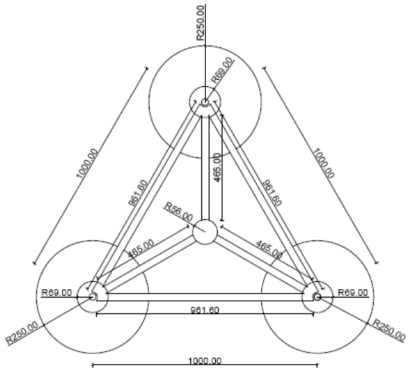

Figure 4.9 Plan dimensions of model floating wind turbine

Table 4.2 Mass and inertia properties for draft = 165 mm

Property	Units	Model Scale	Full Scale
Mass	kg	70.45	8.75E+6
Gravity	m/s^2	9.81	9.81
Vertical CG with respect to the free surface	m	0.238	11.9
Ixx with respect to system CG	$kg.m^2$	23.48	7.338E+9
Iyy with respect to system CG	$kg.m^2$	23.48	7.338E+9
Izz with respect to system CG	$kg.m^2$	23.48	7.338E+9

Table 4.3 Mass and inertia properties for draft = 275 mm

Property	Units	Model Scale	Full Scale
Mass	kg	90	1.125E+7
Gravity	m/s^2	9.81	9.81
Vertical CG with respect to the free surface	m	0.0483	2.415
Ixx with respect to system CG	$kg.m^2$	30	9.375E+9
Iyy with respect to system CG	$kg.m^2$	30	9.375E+9
Izz with respect to system CG	$kg.m^2$	30	9.375E+9

Table 4.4 Mass and inertia properties for draft = 435 mm

Property	Units	Model Scale	Full Scale
Mass	kg	113.5	1.4187E+7
Gravity	m/s^2	9.81	9.81
Vertical CG with respect to the free surface	m	-0.213	-10.65
Ixx with respect to system CG	$kg.m^2$	37.8	1.182E+10
Iyy with respect to system CG	$kg.m^2$	37.8	1.182E+10
Izz with respect to system CG	$kg.m^2$	37.8	1.182E+10

4.3 Measurement Systems

Six degrees of freedom of the floating platform were measured in the wave basin. Measurement systems used in measurement processes;

1. IMU (inertial measurement unit); It enables the measurement of the floating model's rotation modes (yaw, pitch and roll).
2. GoPro Camera ; The floating model's linear movements (surge, sway, and heave) were measured.
3. Load Cell (3 pieces); The tension forces on the mooring systems of the floating model were measured.
4. Data loggers (IMC brand); The data acquisition system analyzes the data from the load cells.
5. Wave Probe; Provides the measurement of the generated waves.
6. Wind generator; The system that provides the effective wind force on the floating platform.

4.3.1 IMU(Inertial Measurement Unit)

By supplying IMU system components, the system in which the roll, pitch and yaw angles will be determined and recorded at selectable intervals up to 500Hz has been created by the project researchers. For this purpose, UM7 sensor and Razor 9DOF IMU sensors given in Figures 4.10a, 4.10b and 4.10cwere used.

(a) General View Of IMU **(b)** UM7 Orientation Sensor **(c)** 9DOF Razor IMU Sensor

Figure 4.10 IMU and sensors

The sensors in Figure 4.10 have a 3-axis accelerometer, 3-axis magnetometer, and 3-axis gyroscope receivers. The Raspberry Pi panel computer was used to convert the received data into Euler angles (roll, pitch, yaw) with the Kalman Filtering to be applied (Figure 4.11).

Figure 4.11 Raspberry Pi panel computer

A code in the Python programming language has been prepared for calculating and recording Euler angles from the data received from the sensors on the Raspberry Pi computer. In addition, the system is supported by an external power bank to eliminate the need for direct connection to the electricity network, thus ensuring uninterrupted operation without the need for any cable connection. With the IMU system, it is possible to determine and record the rotations of the floating model up to a 500 Hz recording range.

4.3.2 Wind Generation System

A drone model was produced in order to provide effective wind force on the floating platform. With the drone model produced, the planned wind forces were produced by remote control on the floating platform. For this purpose, a 6-propeller drone body was used (Figure 4.12).

Figure 4.12 Wind generation system overview

Considering the dimensions and weight of the floating platform, it has been determined that the wind forces that can be effective on the platform can only be produced with a 6-propeller drone model. Together with the body given in (Figure 4.14a), 6 brushless motors are used to provide sufficient power. 6 Sunnysky X4108S

380kv brushless motors, 1355 carbon fiber propellers (Figure 4.14b) , 40A, 6S brushless motor driver(Figure 4.14c), 6 channel 2.4ghz controller (Figure 4.13d) and other equipment such as lipo battery, flight control card were used.

(a) Sunnysky X4108S 380kv brushless motor

(b) 1355 carbon fiber propeller

(c) 40A, 6S brushless motor driver

(d) 6 channel 2.4ghz controller

Figure 4.13 Wind generation drone components

By mounting the drone model on a floating platform, the required wind forces on the platform are produced in the desired direction and intensity.

4.3.3 Load Cell

The load cell was used to measure the mooring tension forces acting on the mooring cables which are attached from the basin floor to the floating body. Each load cell was connected to mooring line and floating body fairlead and placed at an angle of 120°. Signals from the load cell were transferred to the data logger available in the laboratory. The data logger was connected to the computer and the data were evaluated(Figure 4.14).

(a) Load Cell

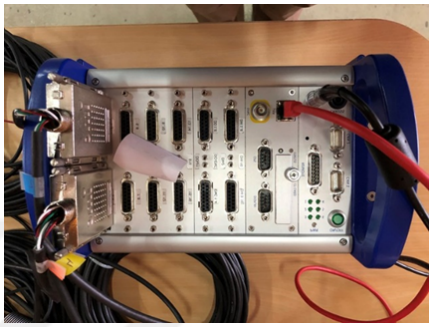

(b) Data Logger

(c) Data Logger and Computer

Figure 4.14 Load cell system

The load cell system was first calibrated using known weights. Four separate load cells were used. Calibration charts are given in Figure 4.15 As can be seen from the Figures, the measurements are sufficiently consistent.

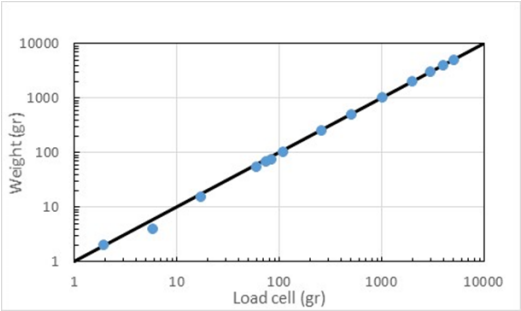

(a) Calibration of Load Cell 1

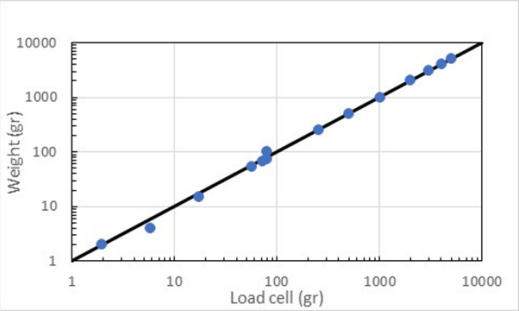

(b) Calibration of Load Cell 2

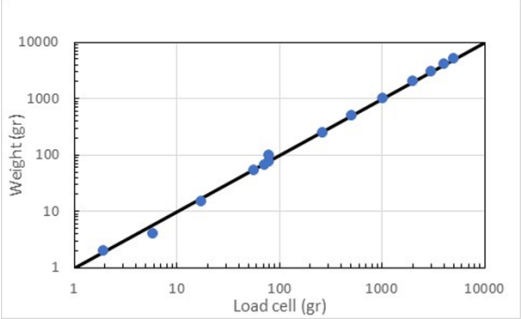

(c) Calibration of Load Cell 3

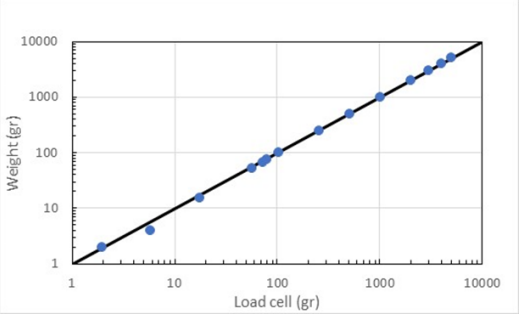

(d) Calibration of Load Cell 3

Figure 4.15 Load cell calibrations

The load cell system is fixed to the basin floor with a stainless connection system, making an angle of 120° symmetrically from three different points of the floating turbine. The layout plan is given in Figure 4.16.

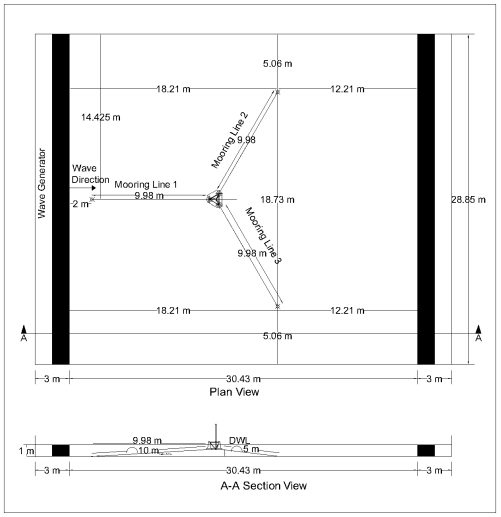

Figure 4.16 Mooring configuration of floating turbine

4.4 Load Case Description

4.4.1 Free Decay Tests

Motion decay tests were carried out on the moored platform to measure its response in the heave, pitch, and surge, modes of motion. The tests were conducted by applying a perturbation force on the platform from a nearby carriage. Free decay test parameters are given in Table 4.5.

Table 4.5 free decay test parameters

Load Case	**Mode**	**Initial Displacement/Rotation**	
		Model Scale	**Full Scale**
FDH275	**Heave**	-0.135 m	6.75 m
FDP275	**Pitch**	-11.38 degree	-11.38 degree
FDS275	**Surge**	0.554 m	27.7 m

4.4.2 Regular and Irregular Wave Tests

Experiments were conducted in moored conditions to investigate the behavior of a structure in regular and irregular waves. The response motions of the platform under irregular waves were investigated. The irregular wave cases were created using wave climate obtained from a study conducted by Islek et al.[38] using 40 years of wind data analysis. The average significant wave height and maximum wave height (for different recurrence periods of 1, 10, and 100 years) for the Western Black Sea will be utilized in this regard. Long-term wave statistics determined in the project area were scaled down using Froude similarity to the model scale, and the wind and wave conditions to be used in the experiments are given in Table 4.6.

Table 4.6 Irregular wave conditions for model and prototype

Load Case	**Prototype**				**Model**			
	H_{m0} **(m)**	L_m **(m)**	T_m **(s)**	T_p **(s)**	H_{m0} **(m)**	L_m **(m)**	T_m **(s)**	T_p **(s)**
W1 (1 Year)	4.03	66.82	6.55	8.18	0.08	1.33	0.92	1.15
W2 (10 Years)	7.48	120.13	8.78	10.98	0.15	2.40	1.24	1.55
W3 (100 Years)	9.09	145.01	9.64	12.05	0.18	2.90	1.36	1.70

The platform was subjected to regular waves with varying wave heights and frequencies and was subsequently analyzed. The parameters of the regular waves utilized in the experiment are presented in Table 4.7.

Table 4.7 Regular wave conditions

Load Case	H (m)	T(s)	f (Hz)
W8R1	0.08	0.8	1.25
W8R2	0.08	0.92	1.09
W8R3	0.08	1.1	0.91
W8R4	0.08	1.18	0.85
W8R5	0.08	1.35	0.74
W15R1	0.15	1.1	0.91
W15R2	0.15	1.24	0.81
W15R3	0.15	1.55	0.65
W15R4	0.15	1.71	0.58
W15R5	0.15	2	0.50

4.4.3 Experimental Results of Regular Wave Tests

In this part, platform motions under regular waves are analyzed, with a focus on two wave outputs: W8R3 and W8R4. To establish a link between the changes in response and variations in wave steepness, the response amplitude operators (RAOs) for the platform's heave and pitch motions were assessed and contrasted.

The Response Amplitude Operator (RAO) is an important component in the design of naval structures, especially floating bodies. It provides critical information about the body's response to regular waves. The RAO is defined specifically as the ratio of the body's motion to the amplitude of the wave that causes that motion. This ratio is usually displayed over a range of wave periods. The RAO can be used to understand how a floating body will respond to varied wave conditions. This data is critical for maintaining the structural integrity, stability, and performance of naval structures like ships, offshore platforms, and floating platforms.

The time series data for the pitch response which is obtained by IMU can be observed in Figure 4.17. In Figure 4.17a, the time series data illustrates the pitch motion under the W8R3 load case, characterized by an 8 cm wave height and a period of 1.10 seconds. Conversely, Figure 4.17b displays the time series data of the pitch motion under the W8R4 load case, which exhibits an 8 cm wave height and a period of 1.18 seconds.

The pitch motion response in both cases demonstrates a regular pattern, as evident

from the time series. Notably, the amplitude of the pitch response is slightly lower for the W8R3 case compared to the W8R4 case. Therefore, it can be concluded that the pitch motion response under regular waves increases with decreasing wave steepness.

The Response Amplitude Operators (RAOs) for the pitch motion in these wave tests are also presented in Figure 4.18. By comparing the RAO values of these two regular wave tests, the observed increase in the pitch response amplitude further supports the conclusion made earlier.

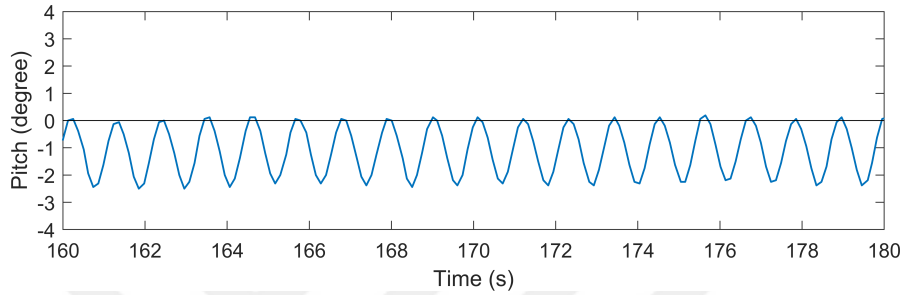

(a) Pitch Time Series of W8R3 load case , Wave Height H=8cm and Wave Period T=1.1 s

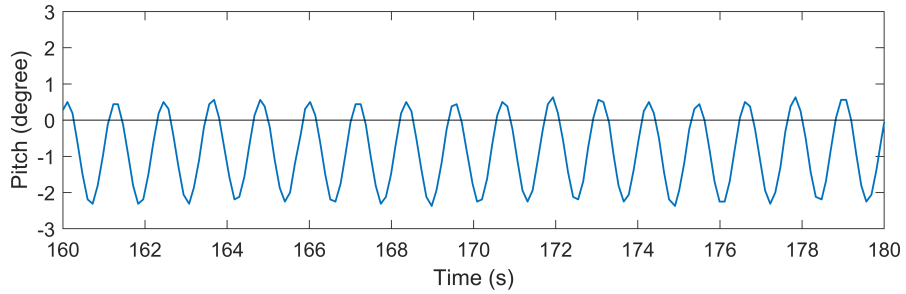

(b) Pitch Time Series of W8R4 load case , Wave Height H=8cm and Wave Period T=1.18 s

Figure 4.17 Time series of pitch motion

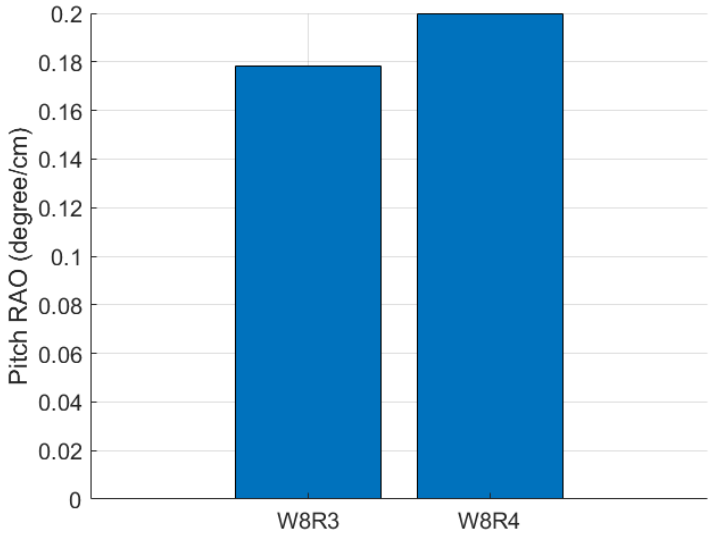

Figure 4.18 Comparison of W8R3 and W8R4 response amplitude operator(RAO)s in pitch motion

The time series of heave data which is obtained by visual processing can be observed in Figure 4.19. In Figure 4.19a, the time series data illustrates the heave motion under the W8R3 load case, characterized by an 8 cm wave height and a period of 1.10 seconds. Conversely, Figure 4.19b displays the time series data of the heave motion under the W8R4 load case, which exhibits an 8 cm wave height and a period of 1.18 seconds.

The heave motion response also demonstrates a regular pattern for both cases, as evident from the time series. Notably, the amplitude of the heave response is much lower for the W8R3 case compared to the W8R4 case. Therefore, it can be concluded that the heave motion response under regular waves also increases effectively with decreasing wave steepness.

The Response Amplitude Operators (RAOs) for the heave motion in these wave tests are also presented in Figure 4.20. By comparing the RAO values of these two regular wave tests, the observed considerable increase in the heave response amplitude further supports the conclusion made earlier.

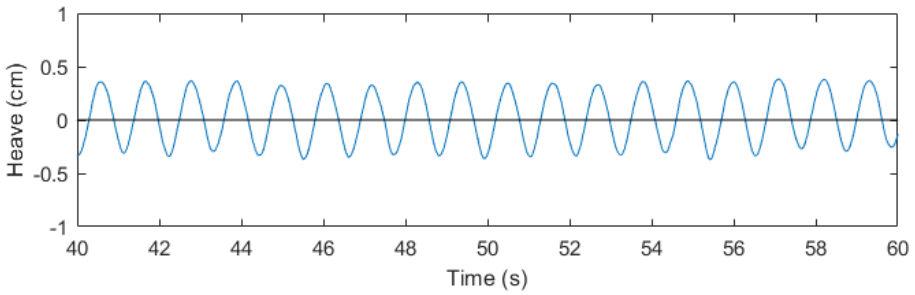

(a) Heave Time Series of W8R3 load case , Wave Height H=8cm and Wave Period T=1.1 s

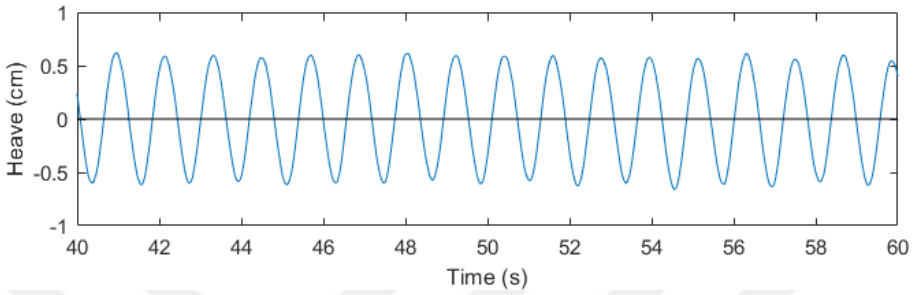

(b) Heave Time Series of W8R4 load case , Wave Height H=8cm and Wave Period T=1.18 s

Figure 4.19 Time series of heave motion

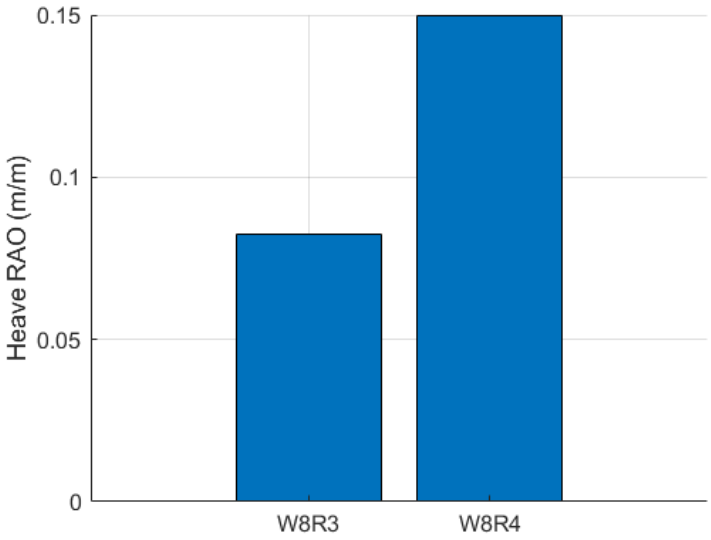

Figure 4.20 Comparison of W8R3 and W8R4 response amplitude operator(RAO)s in heave motion

4.4.4 Experimental Results of Irregular Wave Test

The power spectral density (PSD) of the platform's response under the irregular wave case W1, characterized by a significant wave height of 0.08 m and a peak period of 1.15 seconds, is discussed in this section. Figure 4.22 presents the time series data and PSD plot illustrating the pitch motion of the platform under the W1 irregular wave.

The power spectral density (PSD) of a degree of motion for a floating body subjected to irregular waves can be defined as the frequency domain distribution of energy or power for that particular motion. The dominant frequencies and energy levels can be specified by analyzing the PSD of related degrees of freedom. In order to obtain, PSD, the time series of the data of the motion is first transformed into the frequency domain by using Fourier analysis.

Figure 4.21a demonstrates that the pitch response of the W1 case exhibits significant irregularity. Notably, the peaks observed in the low-frequency range of the PSD align with the pitch natural frequency of the model. Additionally, Figure 4.21b reveals other peaks within the frequency range corresponding to the incident waves.

Figure 4.22 displays the time series data and power spectral density (PSD) of the heave motion of the platform under the W1 irregular wave. It can be observed from Figure 4.22a that the heave response of the W1 case exhibits significant irregularity. The PSD plot reveals peaks at low frequencies that align with the heave natural frequency of the model. Additionally, other peaks can be observed within the frequency range corresponding to the incident waves, as depicted in Figure 4.22b.

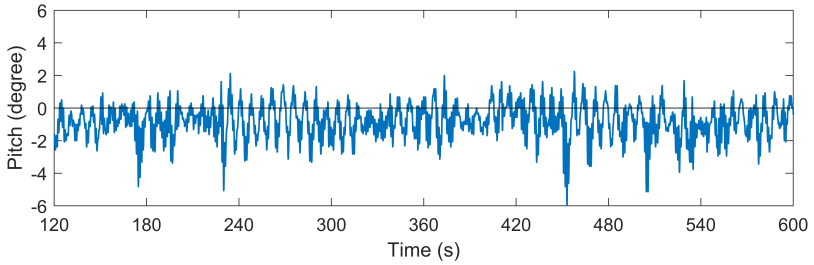

(a) Pitch Time Series of W1 load case , Significant Wave Height H_s=8cm and Peak Wave Period T_p=1.15 s

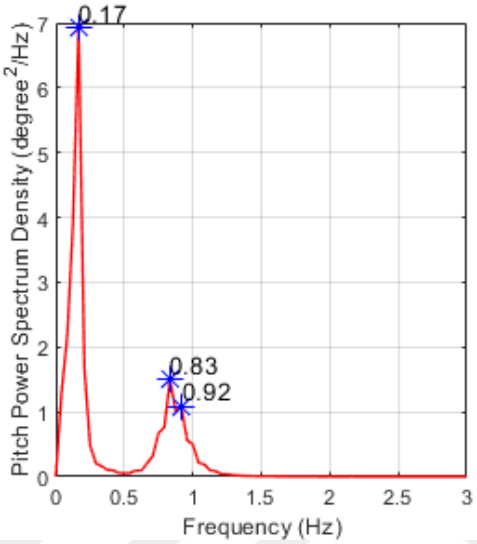

(b) Pitch PSD of W1 load case , Significant Wave Height H_s=8cm and Peak Wave Period T_p=1.15 s

Figure 4.21 Pitch time series and PSD of W1 load case

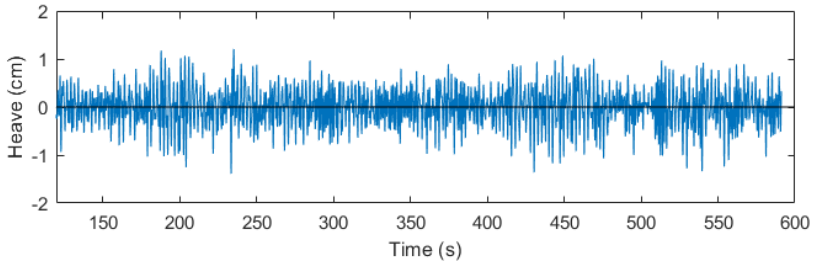

(a) Heave Time Series of W1 load case , Significant Wave Height H_s=8cm and Peak Wave Period T_p=1.15 s

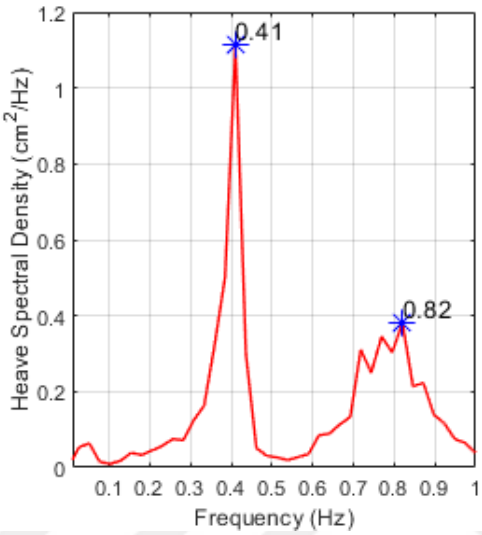

(b) Heave PSD of W1 load case , Significant Wave Height H_s=8cm and Peak Wave Period T_p=1.15 s

Figure 4.22 Heave time series and PSD of W1 load case

5
NUMERICAL MODELLING

5.1 Introduction

In this chapter, the performance of the floating structures subjected to free decay tests and regular waves is further validated using a numerical wave tank. A vertical floating cylinder is the first case to study.

For the first case, the three-dimensional cylinder case is validated by comparing the results to both experimental and validated numerical result data for free heave and pitch decay. The simulation of wave structure interaction of this case is also performed for this case and validated by comparing the results of the studies of Palm et al.[9].

In the second case, the open-source FOWT DeepCWind simulation uses the same numerical settings that were applied to the simple cylinder case to perform free decay tests. For free heave and pitch decay, the case is validated by comparing the results to both experimental and validated numerical result data. The simulation of wave structure interaction of this case is also performed for this case and validated by comparing the results of the studies of Robertson et al.[5].

The new design semi-submersible's free heave and pitch decay tests were also performed and natural periods and damping coefficients in heave and pitch motion is evaluated and compared with the experimental results.

5.2 3D Floating Cylinder

The response of a 3D floating vertical cylinder is investigated throughout this section. The fluid-structure interaction is examined by using overset mesh technique provided by the recent version of OpenFOAM. Firstly, free heave and pitch decay tests are carried out by using OpenFOAM. The result which is obtained by these tests is compared to experimental results data obtained by Palm et al.[9]. A

visualization of the 3D Cylinder case is shown in Figure 5.1.

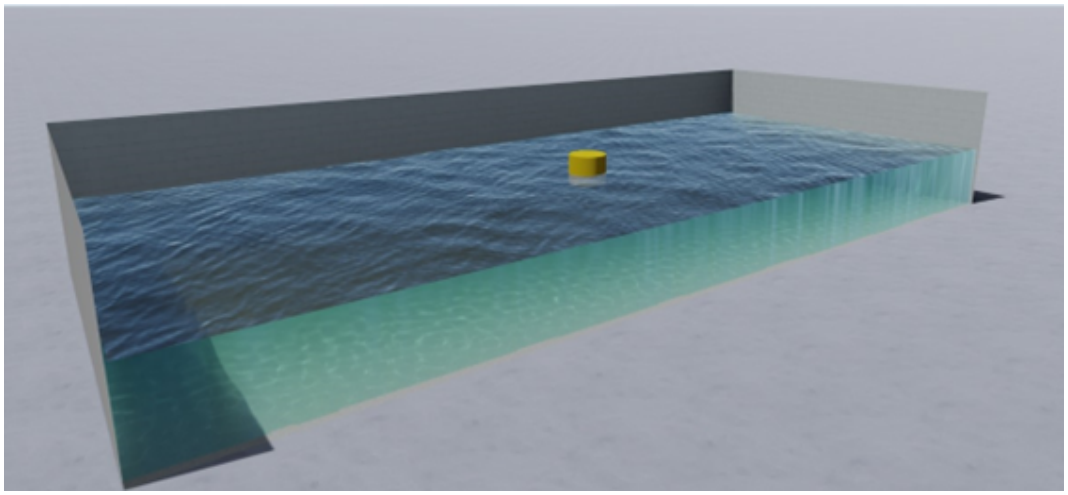

Figure 5.1 Visualization of 3D cylinder case

5.2.1 Case Description

The physical characteristics of the floating object, as reported in the stud of Palm et al.[9], include a cylinder shape with a diameter of 0.515 meters and a height of 0.401 meters, weighing 35.85 kilograms. Additionally, the draft of the free-floating body is stated to be 0.172 meters. Although the water density is not mentioned in the study of Palm et al. [9], it is specified as ρ = 1000.59 kg/m^3 in study of Pinguet et al.[39], in order to attain hydrostatic equilibrium with this draft. This same water density of ρ = 1000.59 kg/m^3 is utilized in the present simulation. The center of gravity (CoG) of the cylinder, located at 0.0758 m above the cylinder's bottom, is also taken into consideration.The moments of inertia of the structure around its center of gravity are $I_{xx} = I_{yy} = 0.9kg.m^2$ and $I_{zz} = 1.18kg.m^2$. The experimental wave tank and the numerical wave tank have the same size. The length, width, and water depth of the numerical wave tank are 12 m, 5 m, and 0.9 m, respectively. The dimensions of the numerical wave tank can be seen in Figure 5.2.

In present study, the meshing process is conducted using the OpenFOAM meshers BlockMesh and SnappyHexMesh. The meshes are created independently and later combined. The global domain's mesh is composed of square cells with a side length of 0.08 m. To refine the mesh near the free surface, the level tool in SnappyHexMesh is employed, with a level 3 refinement implemented around the free surface resulting in cell sizes of 0.01 m. The convergence of the mesh is improved when the size of the cells in the fitted mesh region is consistent with the nearby zone of the background mesh. Thus, a refined zone is also created in the expected movement area of the floating body.

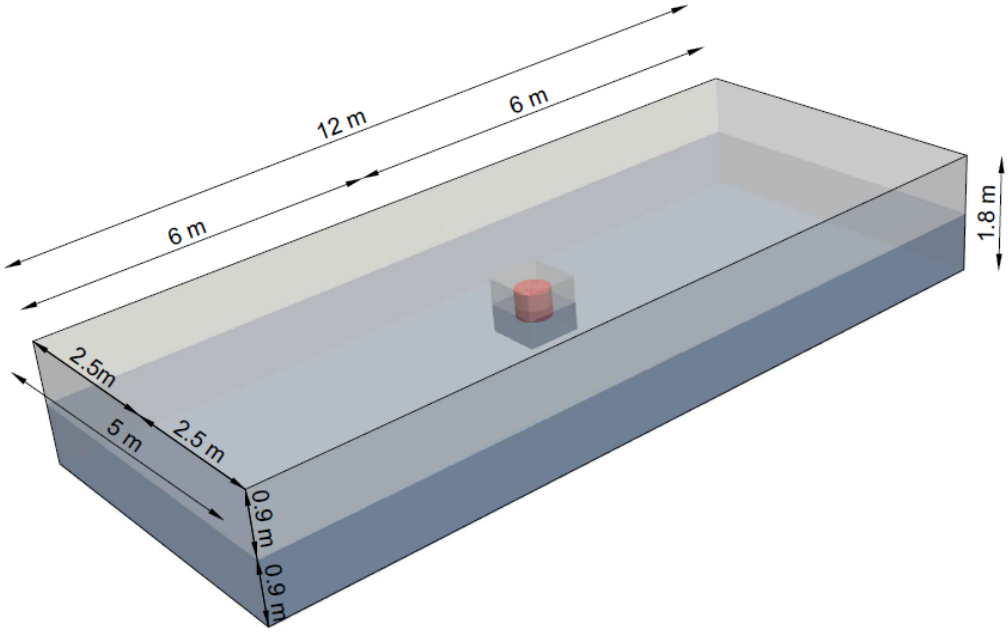

Figure 5.2 Dimensions and overview of the computational domain

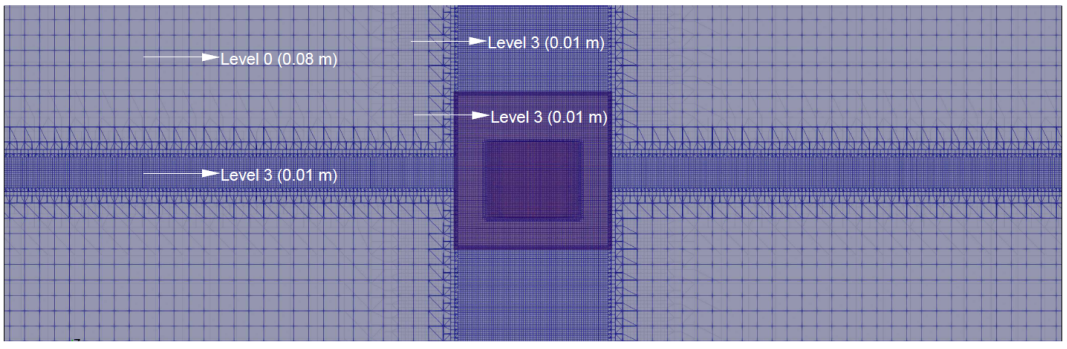

Figure 5.3 Mesh resolution of computational domain

5.2.1.1 Boundary Conditions

This case differs from non-overset cases in that the oversetPatch is subjected to the overset boundary condition. The velocity boundary condition is defined as moving wall velocity around the floating body. The OpenFOAM® user guide has further information about boundary conditions.

Table 5.1 Boundary conditions of 3D floating cylinder free decay tests case

	Alpha (α)	**Pressure (p)**	**Velocity (U)**
FloatingBody	zeroGradient	fixedFluxPressure	Moving wall velocity
Inlet	zeroGradient	fixedFluxPressure	0
Outlet	zeroGradient	fixedFluxPressure	0
Walls	zeroGradient	fixedFluxPressure	0
Ground	zeroGradient	fixedFluxPressure	0
Atmosphere	inletOutlet	totalPressure	Pressure Inlet Outlet Velocity
OversetPatch	overset	overset	overset

5.2.2 Calculation of natural frequencies and damping ratios

To calculate the natural periods and damping ratios, an equation describing a system undergoing free vibration with damping was utilized. The damping ratio was calculated as:

$$\xi = \frac{\delta}{\sqrt{4\pi^2 + \delta^2}} \tag{5.1}$$

δ which is the logarithmic decrement:

$$\delta = \frac{1}{n} \ln \frac{x(t)}{x(t + nT)} \tag{5.2}$$

The variable x(t) represents the difference between the amplitude and the final value of the system at time t, while x(t + nT) refers to the difference between the peak and the final value n periods later, where n is any positive integer representing successive peaks. Three positive peaks (n=3) were used to calculate the natural period and damping coefficients of the motions.

5.2.3 Free Heave Decay Test

To validate the accuracy of the CFD model, a heave decay test was conducted initially. The decay motion was initiated by shifting the Fitted mesh of the floating body by 0.075 m from its theoretical equilibrium position. The vertical

displacement used in the CFD model was kept consistent with the displacement used in the experimental data presented in Palme et al.[9]. Figure 5.4 shows the body's initial displacement.

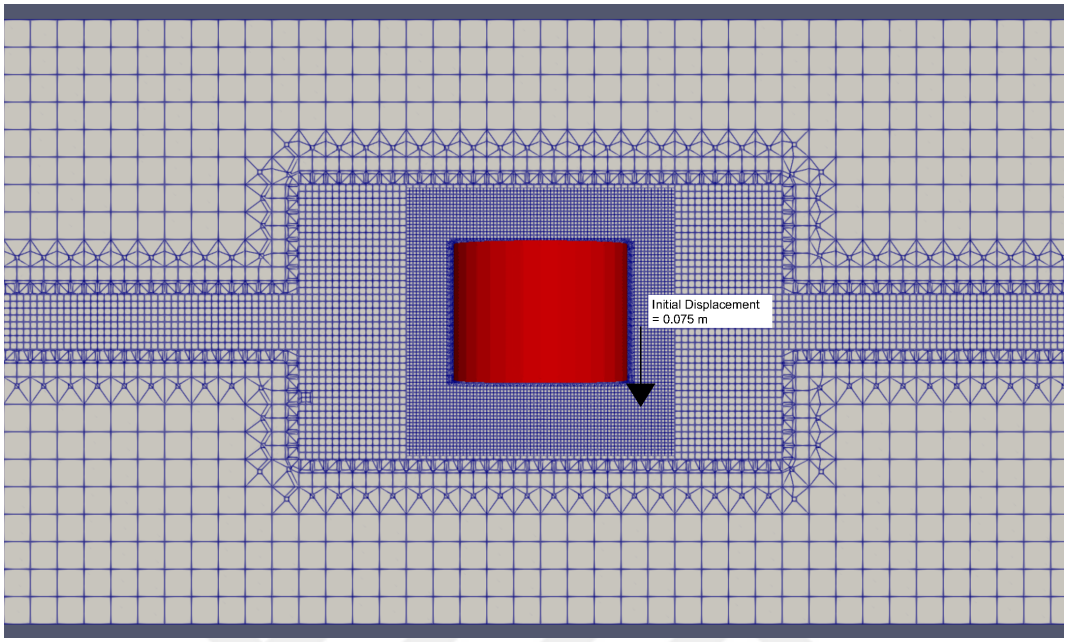

Figure 5.4 Initial displacement of cylinder

The time series plot in Figure 5.5 illustrates a comparison between the experimental results obtained from Palm et al.[9] and the numerical results obtained from this study.

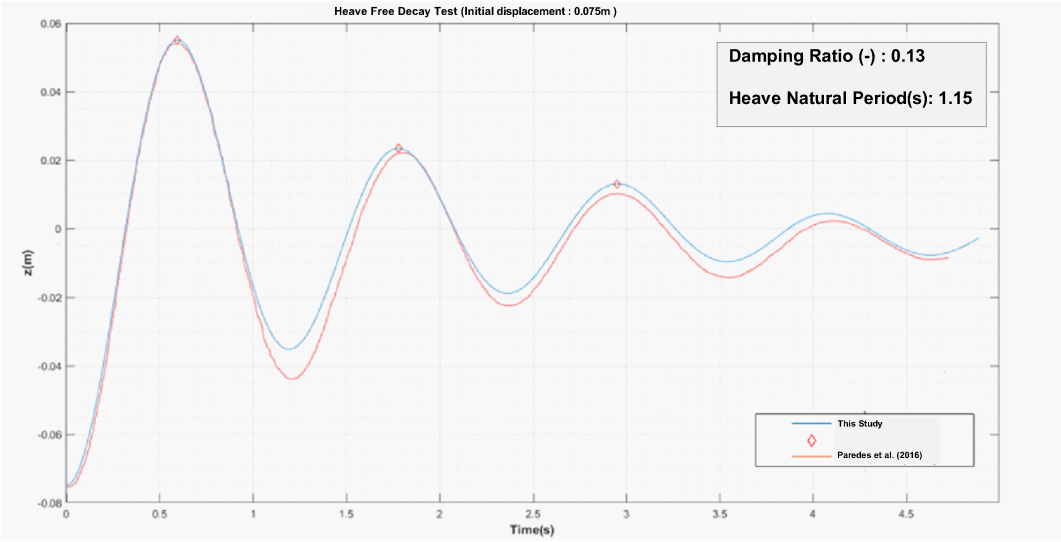

Figure 5.5 Heave decay time series of the experimental results of the Palm et al.[9] and the computational results of this study

The overset mesh approach employed in this study provided exhibited satisfactory agreement with the experimental results, with a period of oscillation of 1.1 seconds,

corresponding to the period of the floating cylinder in heave. The natural period is a crucial parameter in the design of any floating body subjected to wave conditions. It should be noted that the water density used in the simulation was adjusted to achieve the floater's hydrostatic equilibrium, as the exact water density used in the experiments was not specified in the literature. Precise knowledge of the shape, mass, and water density are essential factors that impact the physical behavior of the heave decay test. Various numerical factors can impact the accuracy of the simulation and, as a result, the natural period and damping of the body's oscillation. These factors include the time step, mesh discretization, and numerical schemes. It is important to carefully select these parameters to ensure accurate results and validate the simulation against experimental data.

5.2.4 Free Pitch Decay Test

Results of free-decay tests for the pitch motion have been obtained for the cylindrical structure. To perform this analysis, the cylindrical structure was rotated 8.8° around its center of gravity from the equilibrium position, considering the surrounding mesh area, and the simulation was initiated. The initial rotation angle is the same as the angle used in the studies by [9]. Figure 5.6 shows the body's initial rotation.

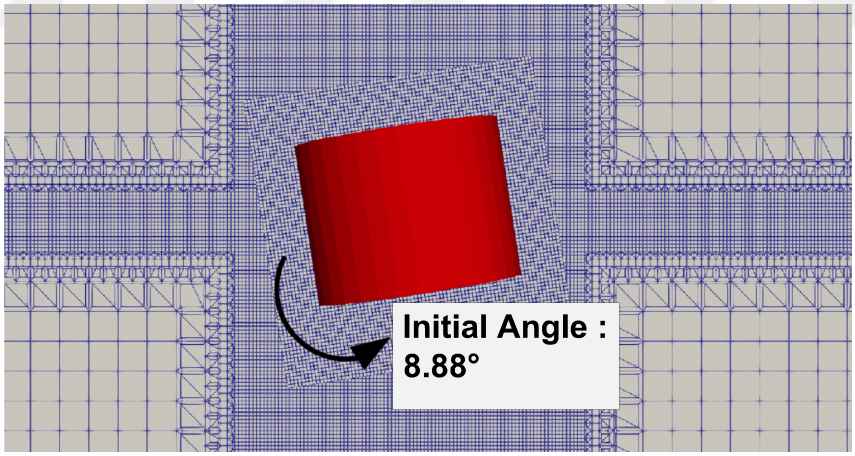

Figure 5.6 Initial pitch rotation of cylinder

The results obtained from the OversetMesh method exhibit strong agreement with the experimental data, with an oscillation period of 1.16 seconds, corresponding to the natural period of the cylindrical structure in pitch motion. The oscillation period in pitch motion is influenced by the inertia and center of gravity position of the structure.

The presented figure, labeled as Figure 5.7, displays a time series comparing the results obtained from the computational model used in this study to the experimental

results obtained in the study of Palm et al.[9].

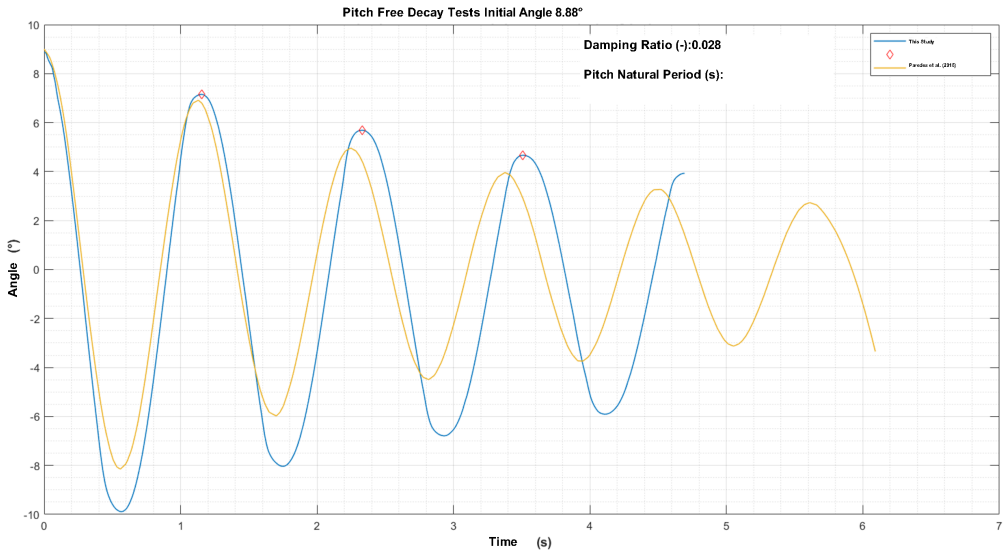

Figure 5.7 Pitch decay time series of the experimental results of the Palm et al.[9] and the computational results of this study

5.3 OC6 Semisubmersible Study

To perform experimental testing on the OC6 project, the MARIN Concept Basin was utilized. This basin has a length of 220 meters, a width of 4 meters, and a depth of 3.6 meters. It is equipped with an overhead carriage that is rigid and extends the full length of the basin. The wave generator used in the study is composed of eight independently operated hinged flaps and technology to compensate for wave reflection. At the downstream end of the basin, a passive wave absorber was installed. The platform used in the experiments consisted of a central cylindrical shaft, three cylindrical legs mounted on circular heave plates, and cross braces connecting all components, including the main shaft, buoyancy legs, and heave plates. The experimental setup of the study Robertson et al.[5] is shown in Figure 5.8.

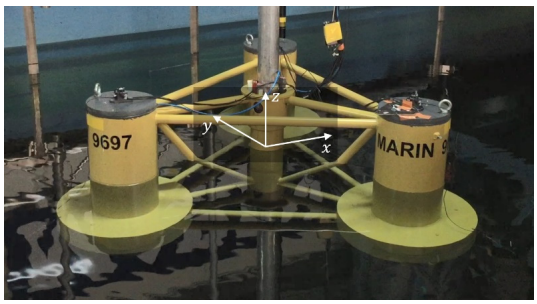

Figure 5.8 Experimental setup of the Robertson et al.[5]

To conduct an additional validation analysis, the experimental results obtained from the OC6 project were utilized. Specifically, the deepCwind floating semisubmersible system was examined by applying free decay test and wave excitations within the scope of the OC6 project. The study presented both the experimental and computational fluid dynamics (CFD) simulation results of the free decay and wave excitation tests of the floating platform, as reported in the OC6 project. To simulate these experimental tests, a computational domain was created in this study. The results of the simulations were compared and validated against the experimental results of the OC6 project.

5.3.1 Case Description

Dimensions and inertial properties of the platform model are given in Table 5.2. The design draft of the model is 0.4 m and the water depth of the computational domain is 3.6 m. All the dimensions that are used in the simulation cases are in the model scale. The dimensions of the computational domain are (-4,4) in the x direction, (-4,4) in the y direction, and (-3.6,2) in the z direction, the origin of the domain coincides with the center of the main column of the model at the free surface. The dimensions of the domain can be seen in Figure 5.9.

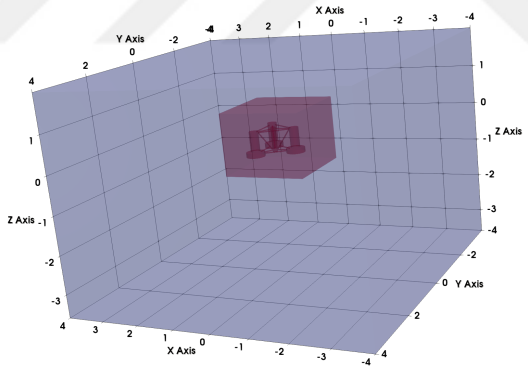

Figure 5.9 Computational domain of DeepCWind free decay test simulations

Table 5.2 Inertial properties of the DeepCwind platform

Property	Units	Model	Prototype
Mass	kg	113.57	1.407E+7
Gravity	m/s^2	9.81	9.81
Vertical CG with respect to the free surface	m	-0.1506	-7.53
Ixx with respect to system CG	$kg.m^2$	41.2736	1.2898+10
Iyy with respect to system CG	$kg.m^2$	41.1232	1.2851E+10
Izz with respect to system CG	$kg.m^2$	45.4048	1.4189E+10

The present study employs two meshing tools, namely BlockMesh and SnappyHexMesh, to create a computational domain for simulating fluid-structure

interactions. To achieve accurate simulation results, the overset mesh discretization technique is implemented, whereby a background mesh and an overset mesh are created independently and then merged. The background mesh consists of square cells with a coarser resolution, with a side length of 0.12 m. However, refinement is applied around the free surface and near the floating body, utilizing level 3 refinement with a side length of 0.03 m. On the other hand, the overset mesh, which encompasses the floating body, comprises square cells with a smaller side length of 0.015 m. This mesh is further refined in the area surrounding the floating body, with a side length of 0.00375 m. Additionally, six boundary layers are constructed around the body surface, with a total thickness of 0.009 m and the first layer having a thickness of 0.0008 m. The mesh resolution of the computational domain is presented in Figure 5.10.

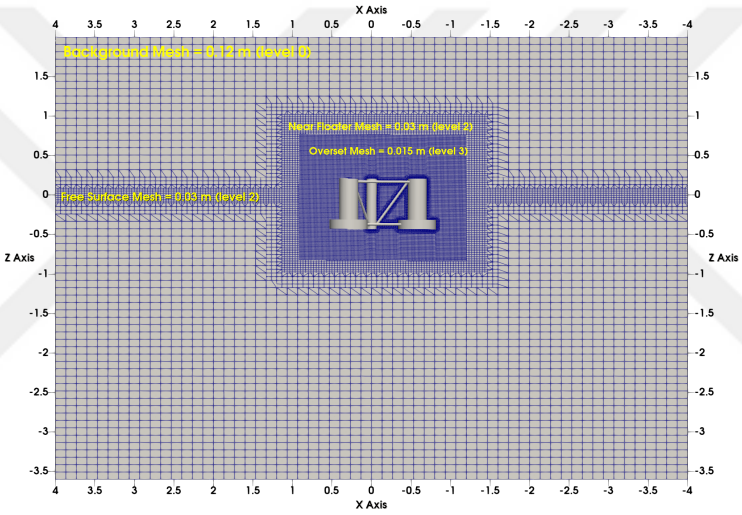

Figure 5.10 Mesh resolution of DeepCWind free decay test simulations

5.3.2 Free Heave Decay Test

In order to verify the accuracy of the CFD model, a heave decay test was conducted first. The decay motion of the floating semi-submersible platform's fitted mesh was initiated by initially displacing it 0.0314 m from its equilibrium position. The vertical displacement imposed in the CFD model was kept consistent with the experimental data from the OC6 project. Figure 5.11 illustrates the initial displacement of the platform.

In this study, the natural periods and damping coefficients were determined by applying the equation of a freely vibrating system with damping and analyzing three positive peak values. The results obtained from the computational test were compared with the experimental data provided by Robertson et al.[5]. The natural

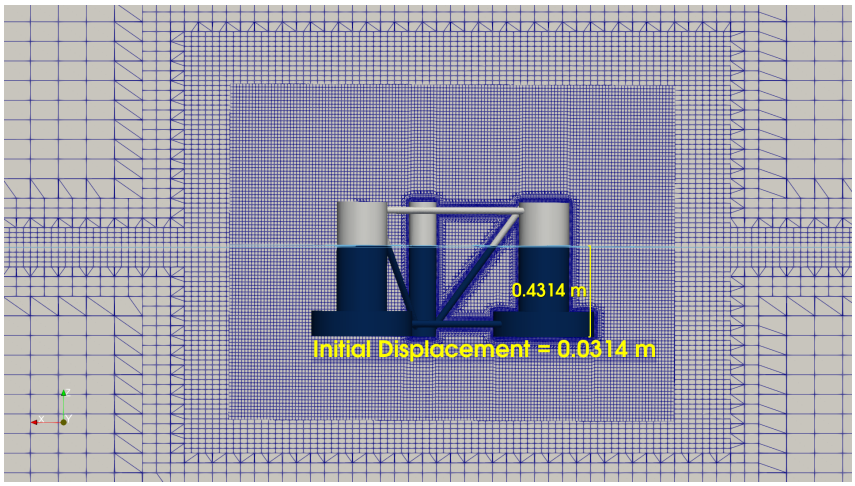

Figure 5.11 Initial position of the DeepCWind heave decay test

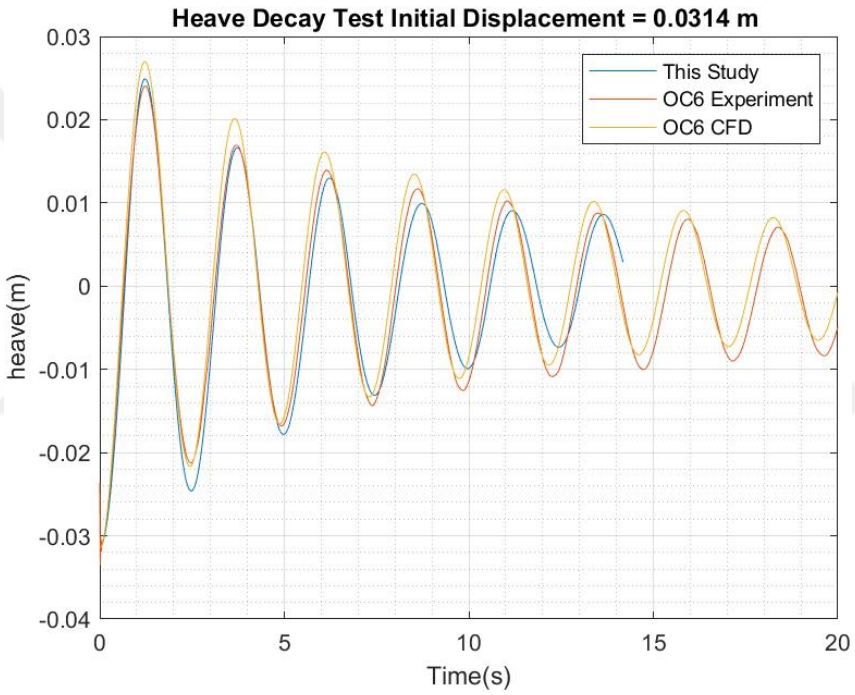

Figure 5.12 Time series of DeepCWind free heave decay test

periods and damping coefficients obtained from the free heave decay tests are compared in Table 5.3.

It was found that the natural heave period of the DeepCWind semisubmersible platform calculated by the CFD simulations showed good agreement with the experimental result, with a negligible error of only 1.6%. However, the heave damping coefficient obtained from the CFD study was observed to be larger than that of the experimental study. This discrepancy could be attributed to the limitations of the mesh and time step resolutions utilized in the simulations. To address this issue, further investigations employing mesh and time convergence

studies could be conducted to eliminate these differences and improve the accuracy of the CFD simulations.

Table 5.3 Comparison of damping and natural periods of OC6 semisubmersible study and this study in heave motion

	This Study	OC6 Experiment	Percent Error (%)
Natural Period (s)	**2.50**	**2.46**	**1.6**
Damping Coefficient (-)	**0.051**	**0.043**	**19.1**

5.3.3 Free Pitch Decay Test

Results of free-decay tests for the pitch motion have been obtained for the semi-submersible platform. To perform this analysis, the semi-submersible platform was rotated 3.95 degrees around its center of gravity from the equilibrium position, considering the surrounding mesh area, and the simulation was initiated. The initial rotation angle is the same as the angle used in the studies by OC6 Experimental study. Figure 5.13 shows the body's initial rotation.

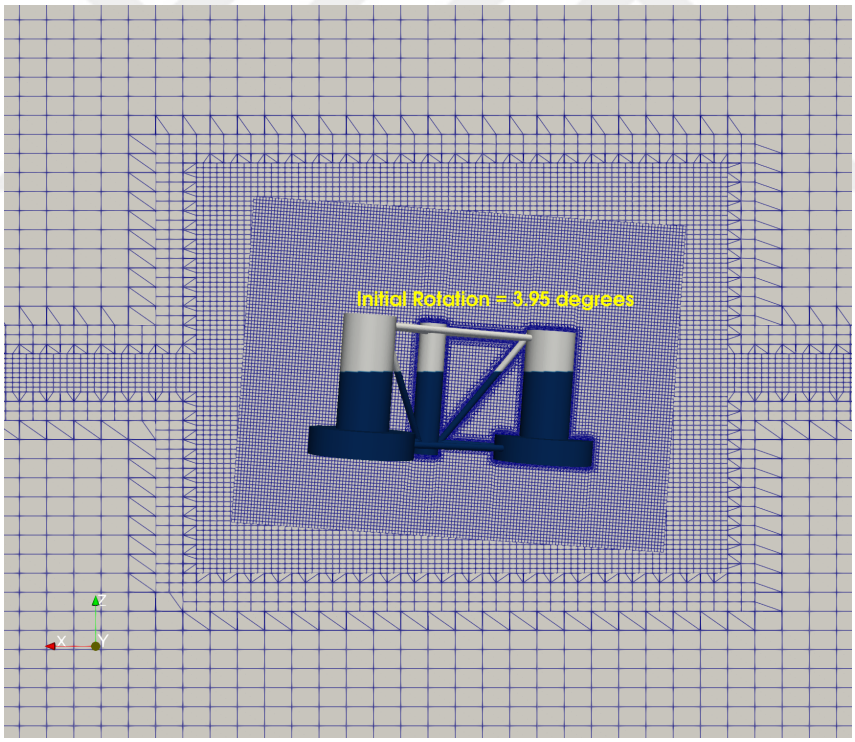

Figure 5.13 Initial rotation of free pitch decay test

In this study, we observed that the natural pitch period obtained from our computational simulations is 10.3% larger than the experimental value. Table 5.4 displays a comparison between the natural periods and damping coefficients of the free pitch decay tests. Additionally, we found that the pitch damping coefficient from our simulations is 31.4% larger than the experimental value. These

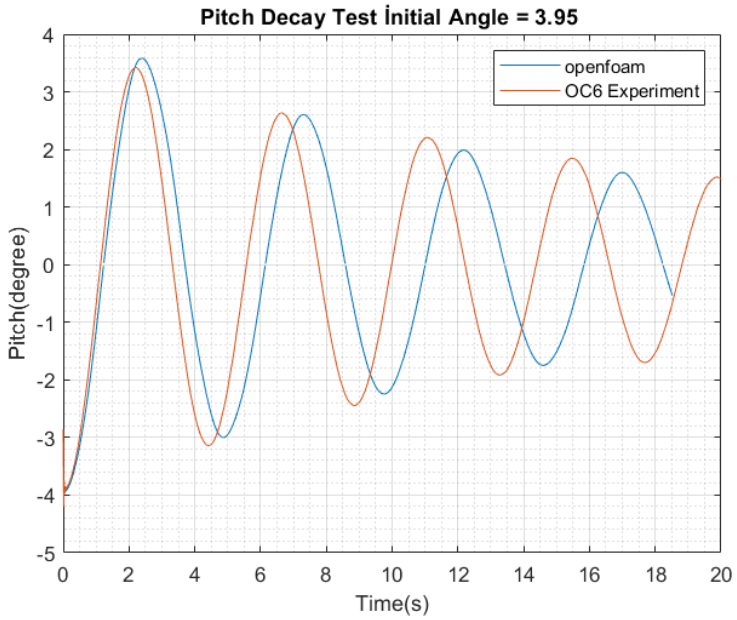

Figure 5.14 Time series of DeepCWind free pitch decay test

discrepancies may potentially be attributed to differences in water density, mass, or center of gravity position compared to the experimental setup.

Furthermore, we suggest that the overestimation of damping coefficients observed in our simulations may also be related to the k-omega SST turbulence model utilized in our analysis. While this model is commonly used in CFD simulations, it has been shown to sometimes result in the overestimation of damping coefficients. To refine our simulation methodology and improve the accuracy of our results, further investigations could be conducted to evaluate the effects of each of these factors on the system's behavior. This would allow for more precise predictions of the system's response, ultimately enabling more effective design and optimization.

Table 5.4 Comparison of damping and natural periods of OC6 semisubmersible study and this study in pitch motion

	This Study	**OC6 Experiment**	**Percent Error (%)**
Natural Period (s)	**4.89**	**4.43**	**10.3**
Damping Coefficient (-)	**0.046**	**0.035**	**31.4**

5.3.4 Regular Wave Tests

The study given in Robertson et al.[5] involved an investigation of the DeepCwind semisubmersible platform's behavior under regular wave conditions. The study constructed a numerical setup in OpenFOAM that replicated the experimental conditions. Within the scope of this part, the results of the computational fluid

dynamics (CFD) simulation were evaluated and validated against the experimental data. This study employed a regular wave with a full-scale wave height of 7.0 meters and a wave period of 12 seconds. To account for the Froude length scale of 1/50, the model wave height and period were reduced to 0.14 meters and 1.697 seconds, respectively. The model water depth was set at 3.6 meters, while the draft of the semisubmersible was 0.4 meters. The study utilized a simplified mooring technique that entailed using three preloaded rigid wires connected to soft springs with a stiffness of 48.9 kN/m at full scale. The inertial properties of the platform are given in Table 5.2. The computational domain is given in Figure 5.15.

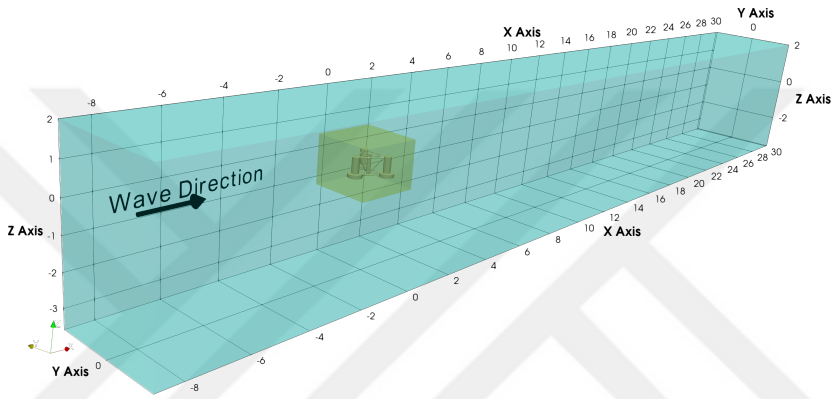

Figure 5.15 Computational domain of DeepCWind semisubmersible for regular wave tests

5.3.4.1 Mesh Refinement

The mesh was optimized at the free surface to accurately depict a semisubmersible structure in a body of water and prevent wave amplitude decay. A box twice the wave height was centered at the free surface level to guide the refinement process. The wave height controlled the mesh size at the free surface, and a ratio of $H/dz = 10$ was utilized to prevent the numerical dampening of the waves. Furthermore, the background mesh near the structure was modified to track the movements of the floater better. The background mesh was created with the blockMesh tool, and the refinement was done with the snappyHexMesh utility. Finally, as described in previous chapters, a boundary layer was created around the surface to improve simulation accuracy. Overall, this method is a well-thought-out and effective strategy for simulating the behavior of a semisubmersible object in a body of water. The mesh regions and mesh refinement is illustrated in Figure 5.16. The yellow area in Figure 5.16 is overset mesh and the blue region is the background mesh.

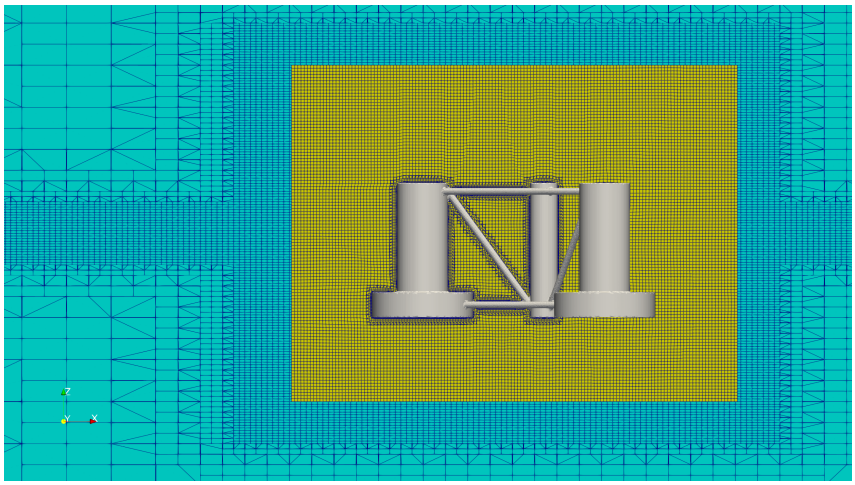

Figure 5.16 Mesh regions and refinement of OC6 semisubmersible case

5.3.4.2 Result and Discussion

The time series comparison of the platform's heave, pitch, surge motion, and tension force of the mooring is given in Figure 5.17.

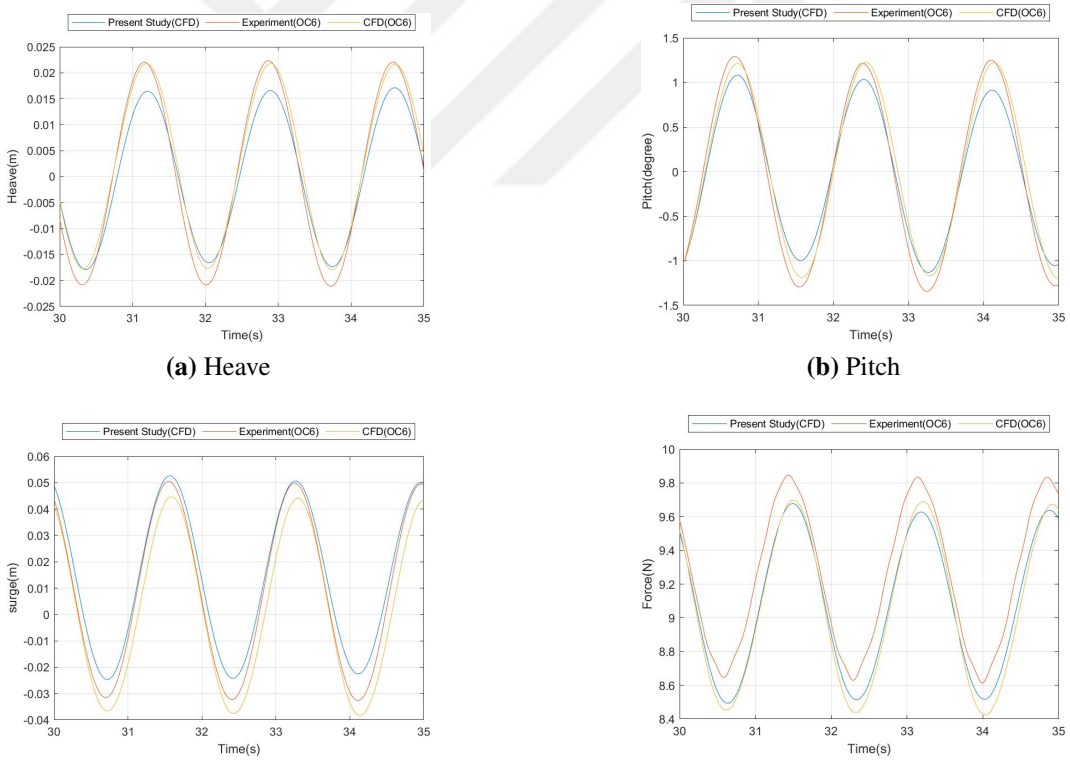

(a) Heave

(b) Pitch

(c) Surge

(d) Mooring Tension

Figure 5.17 Time series comparison of the heave, pitch, surge motion and tension force

The dynamic motions of the platform in heave, pitch and surge DoFs and Tension at the mooring line which is located in the wave direction were obtained by the simulation. Response amplitude operators of the obtained data are presented in this section. The results of the present study is compared with the OC6 experimental measurements and the main simulation result of the OC6 study. The RAOs normalized with the wave amplitude are given in Figure 5.18.

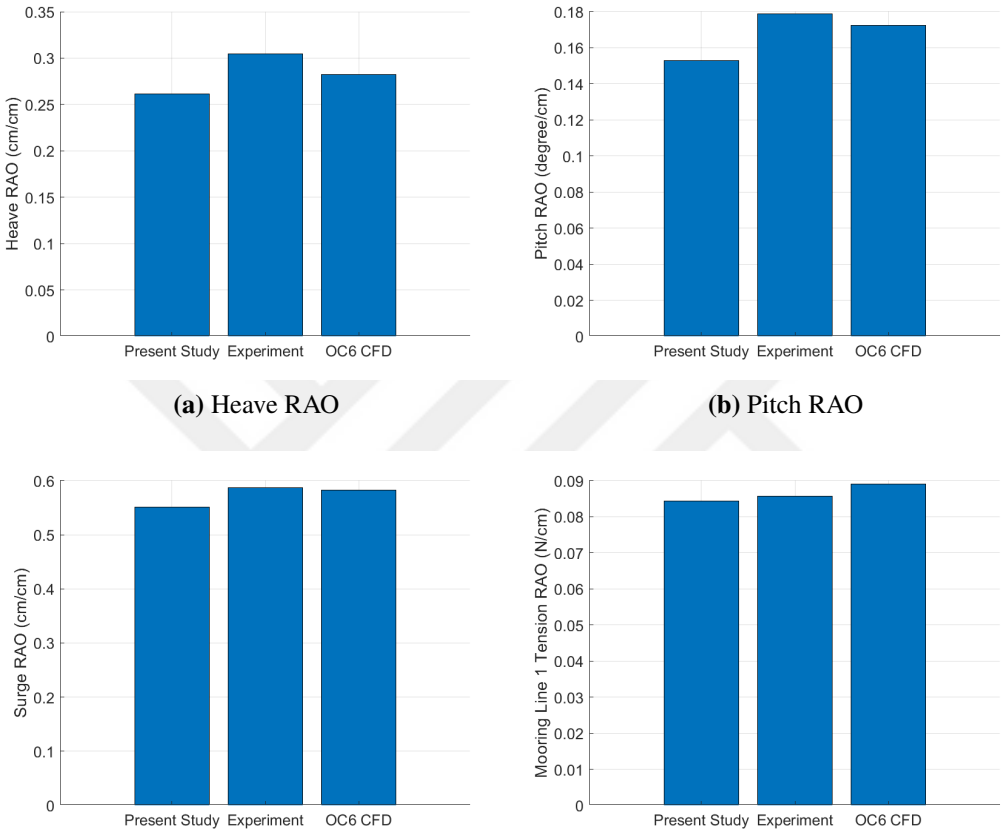

(a) Heave RAO

(b) Pitch RAO

(c) Surge RAO

(d) Mooring Tension RAO

Figure 5.18 RAOs of the heave, pitch, surge motions and tension force of mooring line

The heave motion computed in this study using OpenFOAM demonstrates dicrepencies with the experimental and numerical results of the OC6 study. The present study underestimates the heave amplitude for both the numerical simulation of the OC6 study and the experimental study. The present study underestimates the heave amplitude with a 14.10% relative error with the experimental study and a 7.32% relative error with the OC6 CFD study. This underestimation may be attributed to the numerical damping of regular waves in CFD studies. To achieve improved results, it would be beneficial to conduct a mesh and time-step convergence study.

In both CFD studies, the RAO (Response Amplitude Operator) of the pitch motion is also underestimated. The present study underestimates the pitch amplitude with a 14.50% relative error with the experimental study and an 11.39% relative error with the OC6 CFD study. This underprediction can be attributed to the second-order pitch response in pitch motion. Additionally, there might be a slight variation in the center of gravity between the experimental model and the numerical model.

Regarding the surge amplitude, the present study underestimates both the experimental results and the OC6 study. The present study underestimates the surge amplitude with a 5.85% relative error with the experimental study and a 15.46% relative error with the OC6 CFD study. Furthermore, the mooring tension in the present study underestimates the tension force observed in both the experimental results and the OC6 CFD results. The present study underestimates the mooring tension with a 1.5% relative error with the experimental study and a 5.29% relative error with the OC6 CFD study. To address this discrepancy, adjusting the stiffness of the mooring line, which is associated with the surge motion, could help mitigate the differences.

In summary, the underestimation of various motion amplitudes in OpenFOAM CFD simulations can be attributed to factors such as numerical damping, inadequate mesh resolution, inaccurate boundary conditions, differences in center of gravity, mooring line stiffness, inadequate wave-structure interaction modeling, and numerical errors. To improve the accuracy of predictions, it is recommended to conduct convergence studies, refine mesh resolution, improve boundary conditions, accurately represent physical parameters, validate against experimental or validated numerical data, and consider advanced numerical techniques. These steps can help mitigate the discrepancies and enhance the agreement between simulated and observed results in heave, pitch, surge, and mooring tension.

5.4 Present Model

The experiments for the new design of a semi-submersible platform were conducted in the wave basin of Yıldız Technical University's "Hydrodynamic Research Laboratory," which measures 30.43 meters in length, 28.85 meters in width, and 2.20 meters in depth. The model was tested at a water depth of 1 meter. The platform comprises three cone-shaped legs, each positioned on a circular heave plate. A central shaft, serving as the turbine's support tower, is situated in the middle of the platform. Cross braces connect the main shaft, buoyancy legs, and heave plates. To determine the model's natural periods and damping coefficients, a

series of free decay tests were conducted. Additionally, CFD simulations of the free decay tests were performed to validate the model against the experimental results. This section discusses the numerical simulation setup and presents the obtained results.

5.4.1 Case Description

Dimension and inertial properties of the platform are given in Table 5.5. The design draft of the semisubmersible is 275 mm and the water depth of the computational domain is 3.6 meters. The dimensions of the computational domain are (-4,4) in the x direction, (-4 ,4) in the y direction, and (-3.6,3) in the z-direction. The origin of the domain coincides with the center of the main column at the free surface. The dimensions of the computational domain used for free decay tests of the new design platform are given in Figure 5.19.

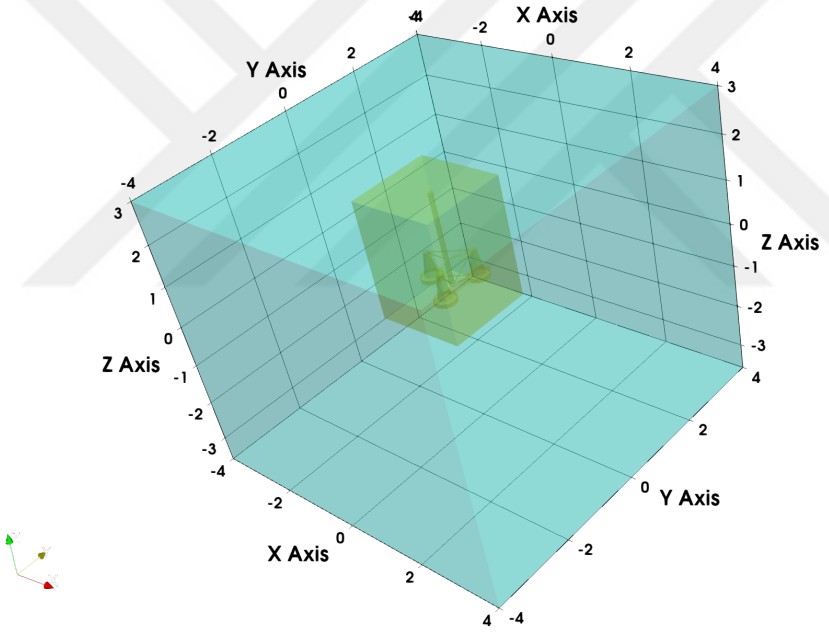

Figure 5.19 Computational domain of new design semisubmersible turbine for Free Decay Tests

Table 5.5 Mass and inertia properties for draft = 275 mm

Property	Units	Model Scale	Full Scale
Mass	kg	90	1.125E+7
Gravity	m/s^2	9.81	9.81
Vertical CG with respect to the free surface	m	0.0483	2.415
Ixx with respect to system CG	$kg.m^2$	30	9.375E+9
Iyy with respect to system CG	$kg.m^2$	30	9.375E+9
Izz with respect to system CG	$kg.m^2$	30	9.375E+9

To refine the mesh for the new design semisubmersible platform, two mesh tools, namely BlockMesh and SnappyHexMesh, were employed. These tools facilitated the creation of a computational domain to simulate fluid-structure interactions. To ensure accurate simulation outcomes, the overset mesh discretization technique was implemented. This involved the independent creation and subsequent merging of a background mesh and an overset mesh.

The background mesh consisted of square cells with a coarser resolution, featuring a side length of 0.12 m. However, refinement was specifically applied around the free surface and near the floating body. This refinement utilized level 3 refinement, employing a side length of 0.03 m. In contrast, the overset mesh, which encompassed the floating body, utilized smaller square cells with a side length of 0.015 m. Further refinement was performed in the region surrounding the floating body, employing a side length of 0.00375 m.

Moreover, to account for boundary effects, six boundary layers were constructed around the body surface. These layers had a total thickness of 0.009 m, with the initial layer having a thickness of 0.0008 m.

The mesh resolution of the computational domain is illustrated in Figure 5.20, showcasing the mesh refinement employed in the Free Decay Test Simulations.

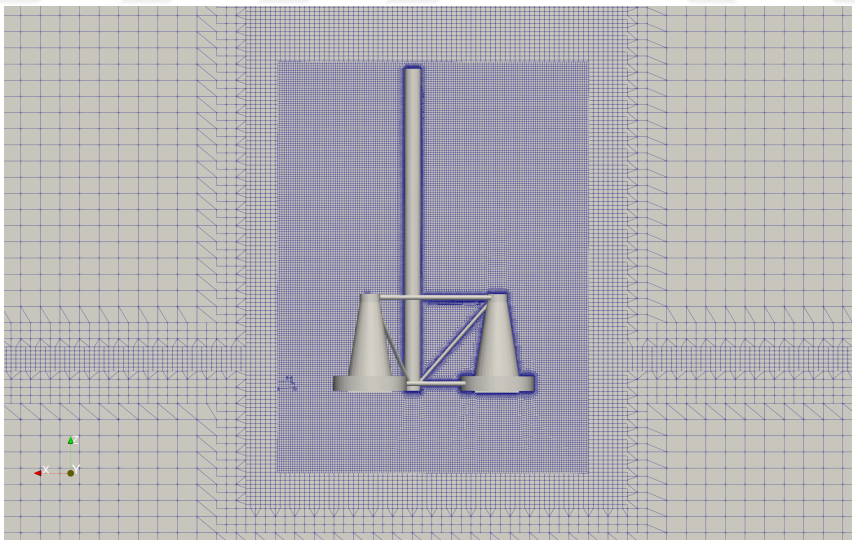

Figure 5.20 Mesh resolution of computational domain for free decay tests of new design semisubmersible

5.4.2 Free Heave Decay Test

A free heave decay test was conducted by displacing the floating platform 0.135 m and then releasing it in the experimental study. For the numerical simulation, the

platform was also displaced 0.135 meters, and the simulation is started. The initial displacement of the platform is given in Figure 5.21. The time series of the heave decay test normalized by the experimental heave natural period of the platform is given in the Figure 5.22.

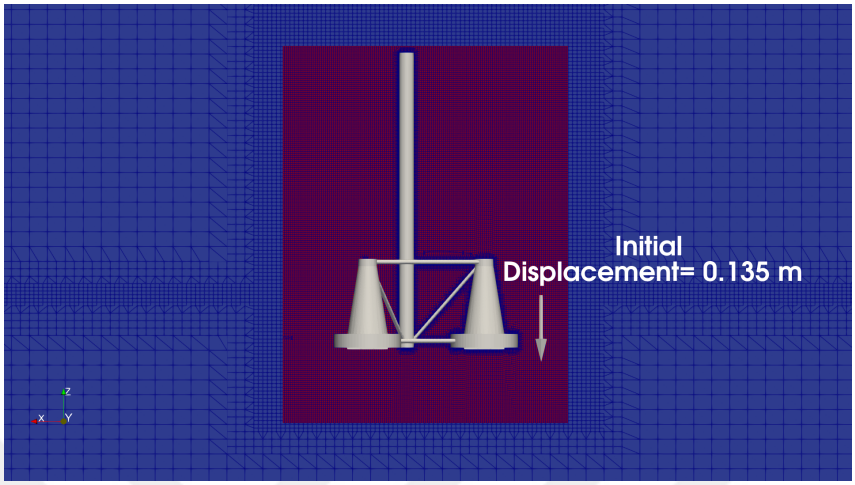

Figure 5.21 Initial displacement of the platform for heave decay test

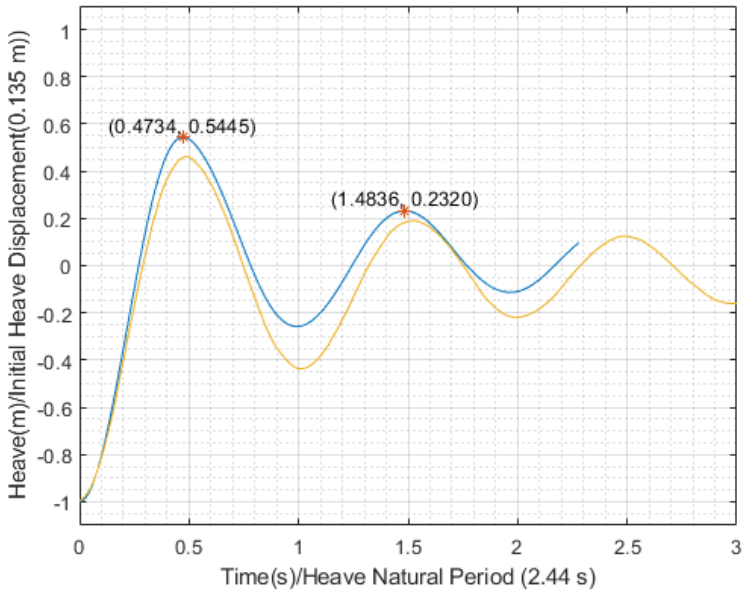

Figure 5.22 Normalized time series comparison of new design platform free heave decay experiment and numerical output

It was found that the numerical natural heave period of the new platform calculated by the CFD simulations showed good agreement with the experimental result, with a negligible error of only 1.19%. However, the heave damping coefficient obtained from the CFD study was observed to be larger than that of the experimental study. This discrepancy could be attributed to the limitations of the mesh and time step resolutions utilized in the simulations. To address this issue, further investigations

employing mesh and time convergence studies could be conducted to eliminate these differences and improve the accuracy of the CFD simulations. The natural periods and damping coefficients obtained from the free heave decay tests are compared in Table 5.6.

Table 5.6 Comparison of damping and natural periods of openfoam and experiment in heave motion

	Openfoam	**Experiment**	**Percent Error (%)**
Natural Period (s)	**2.465**	**2.436**	**1.19**
Damping Coefficient (-)	**0.13**	**0.10**	**30**

5.4.3 Free Pitch Decay Test

A free pitch decay test was conducted by rotating the floating platform 11.38 degrees from its center of gravity and then releasing it in the experimental study. For the numerical simulation, the platform was also rotated around its center of gravity with an angle of 11.38 degrees, and the simulation is started. The initial time series of the pitch decay test normalized by the experimental pitch natural period of the platform is given in Figure 5.23.

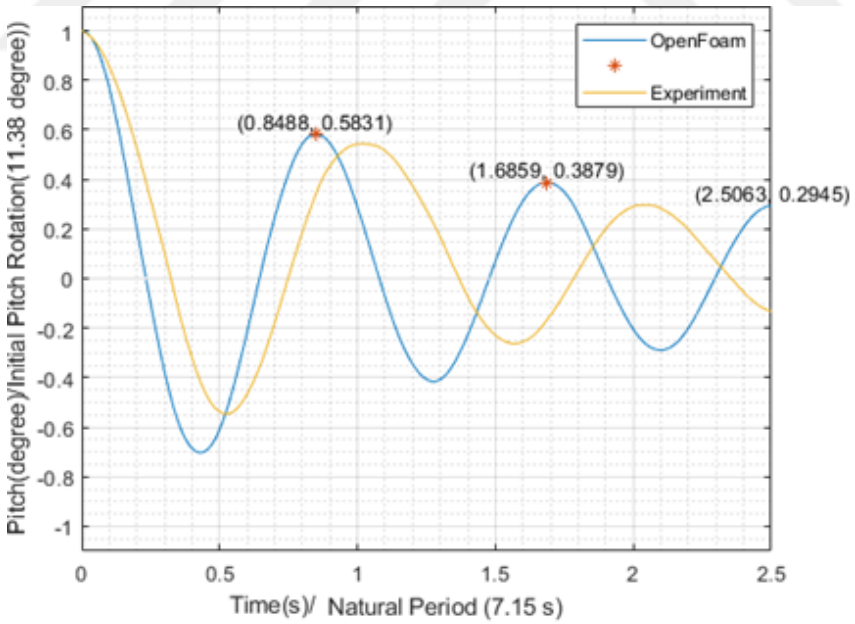

Figure 5.23 Normalized time series comparison of new design platform free pitch decay experiment and numerical output

In this study, we observed that the natural pitch period obtained from our computational simulations is 15.80% shorter than the experimental value. Table 5.7 displays a comparison between the natural periods and damping coefficients

of the free pitch decay tests. Additionally, we found that the pitch damping coefficient from our simulations is 27.71% smaller than the experimental value. These discrepancies show that the location of the center of gravity plays a crucial role in determining coefficients related to pitch motion.

Table 5.7 Comparison of damping and natural periods of openfoam and experiment in pitch motion

	Openfoam	**Experiment**	**Percent Error (%)**
Natural Period (s)	**6.02**	**7.15**	**15.80**
Damping Coefficient (-)	**0.0647**	**0.0895**	**27.71**

6
RESULTS AND DISCUSSION

An experimental study was conducted to determine the natural periods and linear hydrodynamic damping coefficients of a newly designed FOWT (Floating Offshore Wind Turbine) platform. This was achieved by conducting free decay tests on the platform. Furthermore, the dynamic response of the platform was investigated under regular and irregular wave conditions.

The study evaluated the platform's periods in heave, pitch, and surge motions, and it was found that these periods were well beyond the range of wave periods, indicating no risk of resonance in these motions. During the regular wave tests with varying wave steepness, it was observed that both the pitch response amplitude and the heave response amplitude increased as the wave steepness decreased.

The results of the irregular wave tests demonstrated that peaks at low frequencies aligned with the heave and pitch natural frequencies of the model. Additionally, other peaks were observed within the frequency range corresponding to the incident waves. These findings provide valuable insights into the behavior and performance of the newly designed FOWT platform under different wave conditions.

For validation of the numerical model, firstly numerical free decay test of a 3D cylinder was performed and compared against the experimental results of the same geometry. The results obtained from the OversetMesh method exhibit strong agreement with the experimental data with slight discrepancies. The discrepancies indicated were related with the lack of information of the water density used in the experimental study.

Then free decay tests and regular wave tests of the DeepCwind semisubmersible were simulated and compared with the experimental data. While the natural heave period of the platform showed good agreement with the experimental results the damping coefficient was overestimated. To address this issue, performing employing mesh and time convergence studies is suggested to eliminate these

differences and improve the accuracy of the CFD simulations. The pitch period and pitch damping coefficient were also overestimated in the computational study. These discrepancies were potentially be attributed to differences in water density, mass, or center of gravity position compared to the experimental setup.

Furthermore, we suggest that the overestimation of damping coefficients observed in our simulations may also be related to the k-omega SST turbulence model utilized in our analysis. While this model is commonly used in CFD simulations, it has been shown to sometimes result in the overestimation of damping coefficients. To refine our simulation methodology and improve the accuracy of our results, further investigations could be conducted to evaluate the effects of each of these factors on the system's behavior. This would allow for more precise predictions of the system's response, ultimately enabling more effective design and optimization.

The DeepCWind semisubmersible is also investigated under regular waves. The study compared heave, pitch, surge, and mooring tension motion analysis results obtained from OpenFOAM simulations with experimental and OC6 numerical data. Overall, there was good agreement, but a slight underestimation of heave amplitude was observed in both the present study and the OC6 simulation. This discrepancy may be attributed to numerical damping effects in CFD simulations. To enhance accuracy, conducting convergence studies, improving mesh resolution, refining boundary conditions, accurately representing physical parameters, validating against experimental or validated numerical data, and considering advanced numerical techniques are recommended. Additionally, both CFD studies underestimated the pitch response, possibly due to second-order pitch effects and differences in center of gravity. The present study overestimated surge amplitude, while the OC6 study slightly underestimated it, and the mooring tension in the present study underestimated the observed tension force. Adjusting the mooring line stiffness associated with surge motion could help address these discrepancies.

Finally, free decay tests of the newly designed model were simulated using OpenFOAM and compared with experimental results. The comparison revealed that the heave period was obtained with a satisfactory level of accuracy. However, the heave damping exhibited a larger discrepancy, indicating the need for time and mesh convergence to reduce this difference. Additionally, the simulation yielded a shorter pitch period compared to the experimental value, potentially attributed to variations in the model's center of gravity between the numerical and experimental setups. These disparities underscore the sensitivity of the model's center of gravity location in determining the coefficients of pitch motion.

6.1 Further Recommendations

As discussed in the preceding chapters, the CFD results obtained in this study exhibit discrepancies when compared to the experimental data. To address these differences, it is recommended to conduct a mesh and time convergence study. This analysis aims to minimize the disparities between the CFD results and the experimental data.

Moreover, exploring the impact of different turbulence models on the outcomes is crucial. By applying various turbulence models, we can determine the influence of each model. This investigation will enhance our understanding of turbulence modeling within the scope of this study.

To optimize computational efficiency, alternative mesh discretization methods can be considered instead of the overset mesh method. Assessing and comparing the performance of different discretization methods will help in selecting the most suitable approach. This, in turn, will reduce computational costs and improve the overall accuracy of mesh generation.

Furthermore, it is advisable to analyze and compare different wave generation tools available in OpenFOAM. This analysis will aid in identifying the most suitable wave generation tool for CFD simulations in this study. Carefully selecting the appropriate tool is crucial for accurately representing wave behavior and capturing relevant phenomena.

Finally, simulating the turbine thrust using CFD is recommended to investigate the coupled aerodynamics and hydrodynamics effects. This simulation will provide valuable insights into the interaction between aerodynamic forces and hydrodynamic effects. It will contribute to a deeper understanding of the turbine's performance and its interaction with the surrounding fluid.

Implementing these recommendations will enhance the accuracy and reliability of the CFD simulations, thus strengthening the overall findings and conclusions of this thesis.

REFERENCES

[1] T. Ishihara, P. V. Phuc, H. Sukegawa, K. Shimada, Takumi, Ohyama, "A study on the dynamic response of a semi-submersible floating offshore wind turbine system part 1 : A water tank test," 2008.

[2] A. J. Coulling, A. J. Goupee, A. N. Robertson, J. M. Jonkman, H. J. Dagher, "Validation of a FAST semi-submersible floating wind turbine numerical model with DeepCwind test data," *Journal of Renewable and Sustainable Energy*, vol. 5, no. 2, Mar. 2013, issn: 1941-7012.

[3] A. J. Goupee, B. J. Koo, R. W. Kimball, K. F. Lambrakos, H. J. Dagher, "Experimental Comparison of Three Floating Wind Turbine Concepts," *Journal of Offshore Mechanics and Arctic Engineering*, vol. 136, no. 2, Mar. 2014, 020906, issn: 0892-7219.

[4] Q. Cao, L. Xiao, Z. Cheng, M. Liu, B. Wen, "Operational and extreme responses of a new concept of 10mw semi-submersible wind turbine in intermediate water depth: An experimental study," *Ocean Engineering*, vol. 217, p. 108 003, 2020, issn: 0029-8018.

[5] A. Robertson, P. Mucha, F. Wendt, J. Jonkman, "OC6 Phase Ia Definition Document: Validation of Nonlinear Hydrodynamic Loading on the DeepCwind Semisubmersible," Feb. 2022.

[6] OpenFOAM, *The open source cfd toolbox and openfoam user guide*, 2021.

[7] T. Tran, D.-H. Kim, "The coupled dynamic response computation for a semi-submersible platform of floating offshore wind turbine," *Journal of Wind Engineering and Industrial Aerodynamics*, vol. 147, pp. 104–119, Dec. 2015.

[8] A. J. Dunbar, B. A. Craven, E. G. Paterson, "Development and validation of a tightly coupled cfd/6-dof solver for simulating floating offshore wind turbine platforms," *Ocean Engineering*, vol. 110, pp. 98–105, 2015, issn: 0029-8018.

[9] J. Palm, C. Eskilsson, G. Moura Paredes, L. Bergdahl, "Coupled mooring analysis for floating wave energy converters using cfd: Formulation and validation," *International Journal of Marine Energy*, vol. 16, May 2016.

[10] I. Rivera Arreba, "Computation of Nonlinear Wave Loads on Floating Structures," M.S. thesis, 2017.

[11] N. Bruinsma, B. T. Paulsen, N. G. Jacobsen, "Validation and application of a fully nonlinear numerical wave tank for simulating floating offshore wind turbines," *Ocean Engineering*, vol. 147, pp. 647–658, Jan. 2018, issn: 00298018.

[12] *CFD Simulation of Semi-Submersible Floating Offshore Wind Turbine Under Pitch Decay Motion*, vol. ASME 2019 2nd International Offshore Wind Technical Conference, International Conference on Offshore Mechanics and Arctic Engineering, Nov. 2019.

[13] Y. Zhou *et al.*, "Numerical modelling of dynamic responses of a floating offshore wind turbine subject to focused waves," *Energies*, vol. 12, no. 18, 2019, issn: 1996-1073.

[14] H. Chen *et al.*, "Application of an overset mesh based numerical wave tank for modelling realistic free-surface hydrodynamic problems," *Ocean Engineering*, vol. 176, pp. 97–117, 2019, issn: 0029-8018.

[15] L. Wang *et al.*, "Oc6 phase ia: Cfd simulations of the free-decay motion of the deepcwind semisubmersible," *Energies*, vol. 15, no. 1, 2022, issn: 1996-1073.

[16] O. Edenhofer *et al.*, *Renewable energy sources and climate change mitigation: Special report of the intergovernmental panel on climate change*. Cambridge University Press, 2011.

[17] L. Brookes, "Energy efficiency fallacies revisited," *Energy Policy*, vol. 28, no. 6, pp. 355–366, 2000, issn: 0301-4215.

[18] R. Sims *et al.*, "Energy supply," English, in *Climate Change 2007: Mitigation. Contribution of Working Group III to the Fourth Assessment Report of the Intergovernmental Panel on Climate Change. Metz, B.; Davidson, O.R.; Bosch, P.R.; Dave, R.; Meyer, L.A. (eds)*. United Kingdom: Cambridge University Press, 2007, pp. 252–322, isbn: 978-0-511-54601-3.

[19] IEA, "World energy outlook 2019," IEA, Paris, Tech. Rep., 2019.

[20] M. K. Hubbert, "The energy resources of the earth," *Scientific American*, vol. 225, no. 3, pp. 60–73, 1971, issn: 00368733, 19467087.

[21] T. Burton, D. Sharpe, N. Jenkins, E. Bossanyi, "The wind resource," in *Wind Energy Handbook*. John Wiley Sons, Ltd, 2001, ch. 2, pp. 11–39, isbn: 9780470846063.

[22] M. Pasqualetti, R. Righter, P. Gipe, "History of wind energy," in Jan. 2004, pp. 419–433.

[23] GWEC, "Global wind report 2021," Global Wind Energy Council, Brussels, Belgium, Tech. Rep., 2021.

[24] WindEurope, "2020 statistics and the outlook for 2021–2025," WindEurope, Brussels, Belgium, Tech. Rep., 2021.

[25] P. South, R. Mitchell, E. Jacobs, "Strategies for the evaluation of advanced wind energy concepts: Final draft.," Solar Energy Research Institute (SERI), Colorado, Tech. Rep., 1983.

[26] EWEA, "Wind energy, the facts," (EWEA), European Wind Energy Association., Brussels, Tech. Rep., 2009.

[27] B. Bulder *et al.*, "Study to feasibility of and boundary conditions for floating offshore wind turbines," Dec. 2002.

[28] S.-P. Breton, G. Moe, "Status, plans and technologies for offshore wind turbines in Europe and North America," *Renewable Energy*, vol. 34, no. 3, pp. 646–654, 2009.

[29] A. R. Henderson, C. Morgan, B. Smith, H. C. Sørensen, R. J. Barthelmie, B. Boesmans, "Offshore wind energy in europe— a review of the state-of-the-art," *Wind Energy*, vol. 6, no. 1, pp. 35–52, 2003.

[30] S. Butterfield, W. Musial, J. Jonkman, P. Sclavounos, L. Wayman, "Engineering challenges for floating offshore wind turbines," Jan. 2007.

[31] T. Tran, D.-H. Kim, "The platform pitching motion of floating offshore wind turbine: A preliminary unsteady aerodynamic analysis," *Journal of Wind Engineering and Industrial Aerodynamics*, vol. 142, Jul. 2015.

[32] X. Mei, M. Xiong, "Effects of second-order hydrodynamics on the dynamic responses and fatigue damage of a 15 mw floating offshore wind turbine," *Journal of Marine Science and Engineering*, vol. 9, no. 11, 2021, issn: 2077-1312.

[33] S. Lefebvre, M. Collu, "Preliminary design of a floating support structure for a 5 mw offshore wind turbine," *Ocean Engineering*, vol. 40, pp. 15–26, Feb. 2012.

[34] D. Roddier, C. Cermelli, A. Weinstein, "Windfloat: A floating foundation for offshore wind turbines—part i: Design basis and qualification process," vol. 4, Jan. 2009.

[35] A. Robertson, J. Jonkman, "Loads analysis of several offshore floating wind turbine concepts," *Proceedings of the International Offshore and Polar Engineering Conference*, Jan. 2011.

[36] C. Hirt, B. Nichols, "Volume of fluid (vof) method for the dynamics of free boundaries," *Journal of Computational Physics*, vol. 39, no. 1, pp. 201–225, 1981, issn: 0021-9991.

[37] H. Rusche, "Computational fluid dynamics of dispersed two-phase flows at high phase fractions," 2003.

[38] F. Islek, Y. Yuksel, C. Sahin, "Spatiotemporal long-term trends of extreme wind characteristics over the black sea," *Dynamics of Atmospheres and Oceans*, vol. 90, p. 101 132, 2020, issn: 0377-0265.

[39] R. Pinguet, S. kanner, M. Benoit, B. Molin, "Validation of open-source overset mesh method using free-decay tests of floating offshore wind turbine," Oct. 2020.

PUBLICATIONS FROM THE THESIS

Conference Papers

1. İnal ve diğ. "Yüzer Yapının Serbest Dalıp Çıkma ve Baş Kıç Vurma Hareketlerinin OpenFOAM ile Sayısal Modellenmesi" Türkiye İnşaat Mühendisliği 18. Teknik Kongre ve Sergisi. İstanbul: İnşaat Mühendisleri Odası, 2022. 409-417.